Status T2K-LAr document

André Rubbia, 17th February 2005

Reminder

- The groups interested in LAr TPC technique are writing a "comprehensive" and "scientific" document on the possibility of having a ≈100 ton LAr TPC @ T2K 2km. No limit on pages. Loose deadline Spring 2005.

- The T2K Collaboration has set as goal to write a TDR with an "Appendix" for the 2km. Boundary conditions: 10 pages LAr detector + 20 pages WC+LAr+MRD physics. Total < 50 pages. Deadline: March ≈10th

- Strategy: we write our comprehensive document and extract relevant material for the 2km appendix.

What we have

- A preliminary abstract
- A preliminary author list
- A basic table of content (outline)
- A certain number of sections
- A certain number of figures

What is the status

- Introduction (Section 1) is OK
- Physics (Section 2) is OK
- Motivation for 100 ton LAr (Section 3) is OK
- Detector overview (Section 4) needs more work
- Cryostat (section 5) needs more work
- Argon process (section 6) needs more work
- Argon monitoring (section 7) needs more work
- Inner detector (section 8) needs more work
- Readout electronic (section 9) needs more work
- Logistics and installation (section 10) is empty
- Detector operation (section 11) is empty
- Detector performance (section 12) needs more work
- Physics program (section 13) needs more work
- Integration with other detectors (section 14) is empty
- Schedule and planning (section 15) is empty
- Cost, funding and responsibilities (section 16) is empty (might be removed)
- Conclusions (section 17) is empty
- References exist but incomplete

Conclusion

- Comprehensive LAr document progressing (now ≈70pages)
- It will not be finished by March 10th
- However, we have enough material to extract for our 2km Appendix (10 pages LAr + physics) and plan to provide it as soon as possible.

February 17, 2005

THE T2K-LAr PROJECT

A Liquid Argon Time Projection Chamber Detector
for the T2K Neutrino Experiment

Abstract

We propose the use of a 100 ton fiducial-mass liquid Argon (LAr) Time Projection Chamber (TPC) as fine-grained detector for the 2 km site of the T2K neutrino experiment that exploits the neutrino off-axis beam of the JPARC facility in Japan. This detector would profit of the distinctive features of the liquid Argon technique to realize a fully active, homogeneous, high-resolution device to be operated in conjuction with a $\sim$ 1 kton Water Cerenkov detector and a muon ranger. A LAr TPC would provide means to perform an independent measurement of ν_μ CC events of the JPARC neutrino flux, a measurement of ν NC events with clean π^0 identification for an independent determination of systematic errors on the NC/CC ratio, the measurement of the intrinsic ν_e CC background, and, last but not least, the collection of a large statistical sample of neutrino interactions in the GeV region for the study of the quasi-elastic (QE), deep-inelastic (DIS) and resonance modelling and of nuclear effects. The proposed LAr TPC design takes largely advantage from the experience gathered by the ICARUS program in many years of R&D. However, innovative features and recent technological advances are well included in the detector implementation for the T2K experiment. In particular, we adopt for the design of the cryostat the internationally recognized codes for the design of conventional cryogenic-fluid pressure storage-vessels as covered in the ASME Boiler & Pressure Vessel Code, Sect. VIII (www.asme.org). Design and construction of the cryostat according to these standards should ensure a reliable and safe cryogenic operation.

Author list

E. Aprile, K. Giboni, M. Yamashita
Columbia University, Nevis Labs, 136 S. Broadway, Irvington, NY 10533, USA

D. Autiero, Y. Declais
Institut de Physique Nucleaire de Lyon, Université Claude Bernard Lyon-1, 4, rue Enrico Fermi 69622 Villeurbanne cedex, France

A. Bachmann, A. Badertscher, A. Baer, Y. Ge, M. Laffranchi, A. Meregaglia, M. Messina, A. Rubbia
Institute for Particle Physics, ETH Hönggerberg, Zürich, Switzerland

A. Bueno, S. Navas-Concha
Departamento de Física Teórica y del Cosmos & Centro Andaluz de Física de Partículas Elementales (C.A.F.P.E.), Universidad de Granada, Spain

F. Cavanna, G. Piano Mortari
Dipartimento di Fisica e INFN, Università dell'Aquila, via Vetoio, L'Aquila, Italy

A. Curioni, B.T. Fleming
Yale University, Sloane Physics Lab 217 Prospect Street, PO Box 208120, New Haven, CT 06520-8120, USA

A. Ereditato
INFN Sezione di Napoli e Dipartimento di Scienze Fisiche, Universita' Federico II, via Cinthia, 80126 Napoli, Italy

I. Gil-Botella, P. Ladrón de Guevara, L. Romero
CIEMAT, Departamento de Fusión y Física de Partículas Elementales, Avenida Complutense 22, E-28040 Madrid, Spain

J. Holeczek, J. Kisiel
Institute of Physics, University of Silesia, Katowice, Poland

D. Kiełczewska, E. Rondio
A.Sołtan Institute for Nuclear Studies, Warszawa, Poland

G. Mannocchi[1]
Laboratori Nazionali di Frascati (LNF), INFN, Frascati, Italy

O. Palamara
Laboratori Nazionali di Gran Sasso, INFN, s.s. 17bis, km 18+910, Assergi (AQ), Italy

P. Picchi[2]
Dipartimento di Fisica, Università di Torino, Torino, Italy

J. Sobczyk
Institute of Theoretical Physics, Wrocław University, Wrocław, Poland

A. Szelc, A. Zalewska
H.Niewodniczański Institute of Nuclear Physics, Kraków, Poland

[1] Also at IFSI del CNR, sezione presso LNF.
[2] Also at Laboratori Nazionali di Frascati (LNF), INFN, Frascati, Italy and IFSI del CNR sezione presso LNF.

Contents

1 Introduction

1.1 Long baseline accelerator neutrino oscillation experiments

The K2K experiment [36] in Japan can be considered as the 'mother' of all long baseline (LBL) experiments, designed and successfully operated to first confirm with artificial neutrinos the oscillation signal found with neutrinos of atmospheric origin [3]. The Super-Kamiokande detector [2] is hit by the low energy neutrinos ($\sim$ 1 GeV) from KEK after a travel of about 250 km. The L/E of the experiment is such to provide adequate sensitivity to the oscillation parameter of the atmospheric neutrino signal. Neutrino oscillations are detected with a ν_μ disappearance experiment profiting of a series of near detectors used for flux normalization and background estimate. The comparison of near/far event rates and the analysis of the energy spectrum distortion are exploited to infer the oscillation signal. The results of the experiment well agree with those obtained by Super-Kamiokande exposed to atmospheric neutrinos, confirming the oscillation hypothesis at nearly the 4σ level [4].

The next LBL experiment to come on duty in 2005 will be MINOS [5] in the NuMI neutrino beam from Fermilab to Soudan Mine, 730 km away from the neutrino target. Also in this case, a ν_μ disappearance search will be performed. The main goal of the experiment is the narrowing down of the errors on the $\sin^2\theta_{23}$ and Δ_{23} oscillation parameters.

By 2006 the CNGS neutrino beam from CERN to LNGS will be commissioned. In this case, one will deal with high energy neutrinos (10-20 GeV). This is needed to be well above threshold for τ production, as required to perform a $\nu_\mu \rightarrow \nu_\tau$ appearance search, following the indications from the atmospheric neutrino measurements that largely favor this oscillation channel. Together with the ICARUS experiment [7], the dedicated OPERA experiment [8] is being built at LNGS, exploiting nuclear emulsions for the direct detection of the short τ track.

The main goal of the next generation of LBL experiments will be the discovery of the third so far unknown angle of the neutrino mixing matrix: θ_{13}, for which only a limit exists set by the CHOOZ reactor experiment [6]. This is one of the principal task of the T2K experiment in Japan [9]. The experiment will make use of the high intensity neutrino beam from the JPARC 50 GeV proton synchrotron (PS) and Super-Kamiokande as a far detector. The baseline length is 295 km. The 0.75 MW beam power of the JPARC PS corresponds to an intensity of about 3.3 $\times$ 10^{14} protons every 3.5 seconds. In order to reach the design sensitivity in the measurement of the mixing parameter, the experiment assumes 130 days of operation at full intensity for five years. The T2K neutrino beam is operated in an off-axis mode. The peak neutrino energy is set to about 0.8 GeV, in order to maximize the sensitivity to the first oscillation maximum of atmospheric neutrinos.

The T2K project is divided into two phases. In the first one mentioned above, the main goal is the precision measurement of neutrino oscillation with a 0.75 MW beam power and Super-Kamiokande as a far detector. In particular, the experiment aims at an order of magnitude better precision in the $\nu_\mu \rightarrow \nu_\tau$ oscillation measurement ($\delta(\Delta m^2_{23}) = 10^{-4}$ eV^2 and $\sin^2 2\theta_{23}$ with 1% precision), a factor of 20 more sensitive search in the $\nu_\mu \rightarrow \nu_e$ appearance ($\sin^2 2\theta_{13} > 0.006$), and a confirmation of the $\nu_\mu \rightarrow \nu_\tau$ oscillation or discovery of sterile neutrinos by detecting neutral current (NC) events. In a second phase, the power of the neutrino beam could be increased (up to 4 MW) and a new far detector could be considered, namely the Hyper-Kamiokande detector [9].

In its final configuration, the T2K experiment will consist of four detector sites, at a distance of 140 m, 280 m, 2 km and 295 km from the neutrino source, respectively. In the first station, muon monitors measure the direction of the proton beam by detecting high energy muons passing through the hadron beam dump. The proton beam direction can be monitored with an accuracy

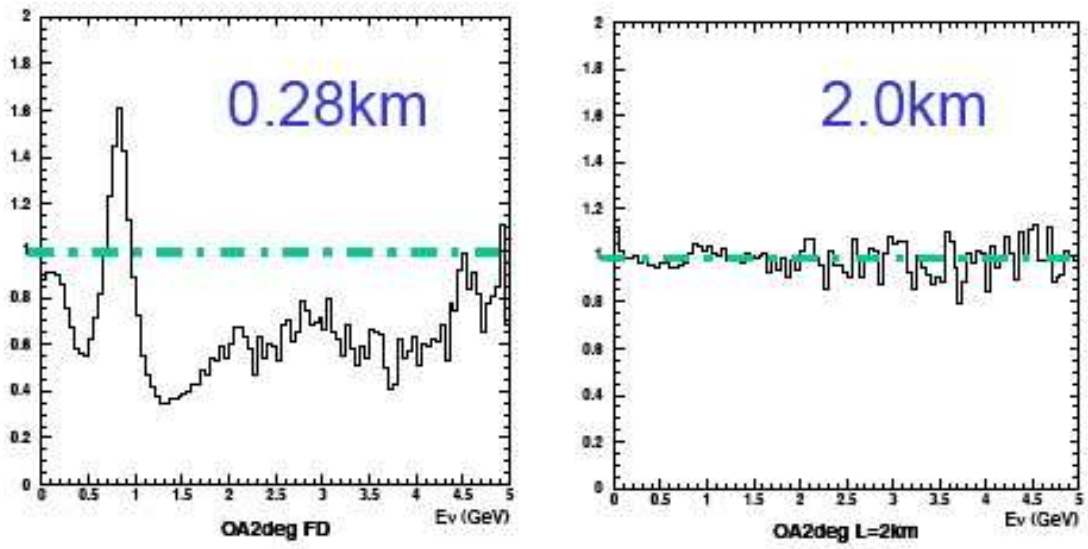

Figure 1: Ratio between the neutrino energy spectra expected at the T2K 280 m (2 km) and far (Super-Kamiokande) detector sites.

better than 1 mrad for each spill by means of segmented ionization chambers and semiconductor detectors.

The second apparatus is located at 280 m from the neutrino target in an experimental hall with a diameter of 20 m and a depth of 40 m, such to cover the on- and off-axis angles between 0 and 3 degrees. The main task of this setup is to provide predictions of the expected neutrino flux at the far Super-Kamiokande detector. The near detector is required to identify both event types (QE, inelastic, NC events) and to measure the neutrino spectrum. A fully-active fine-grained scintillator tracker, similar to the one for the K2K upgrade, is being considered as a candidate for the near detector at 280 m. With sufficient granularity, the detector can fully reconstruct QE scattering events by tagging the recoil protons, and identify pions from inelastic scatterings. The detector should have enough radiation length to measure the energy and the direction of electrons from the electron-neutrino interaction and neutral pions from NC reactions. Ideally, all systematic uncertainties cancel out by using the measured spectra in the near detector. In the real case, near detectors differ from the far detector in terms of material, size and response. The closer location to the decay pipe also introduces a large and complicated far-to-near spectrum ratio, as shown in Fig. 1.

A natural solution to the above problem is to place another set of detectors further away from the production target (off-axis), with the goal of achieving the ultimate control of systematic errors arising from the extrapolation of the 'near' neutrino spectra to the far detector. This can be done by detecting neutrino interactions at a position where the neutrino spectra are similar to those at Super-Kamiokande, so that the various systematics cancel by taking the far-near ratio. The baseline option foresees to construct a water Cerenkov detector at a 2 km distance site.

From event rate considerations, the fiducial mass of this intermediate detector must be about 100 tons, corresponding to a water tank with a total volume of about 9 m in diameter and 15 m in length, for a total weight of 1000 tons.

In addition to the water Cerenkov detector, it is required to install a downstream muon

ranger to measure the energy of penetrating muons that are produced by the high energy tail of the neutrino flux. Last but not least, a fine-grained detector has to be operated in combination with the water Cerenkov detector in order to study the details of neutrino interaction kinematics down to low energy.

This latter detector is the subject of the present document. We propose and assess the feasibility of a $\sim$ 100 ton fiducial mass liquid Argon Time Projection Chamber detector for the precision measurement of neutrino interactions in the 2 km near station of T2K [29].

1.2 Previous experience with liquid Argon TPC

Already in the 60's the potentials of liquid noble gases to realize position sensitive detectors with high spatial resolution was recognized (see *e.g.* [15]). R&D work led to the possibility of using these gases for performing calorimeters for particle physics experiments (see *e.g.* [16]). Among the various ideas developed around the use liquid noble gases, the Liquid Argon Time Projection Chamber [17] certainly represented one of the most challenging and appealing designs. The operation of the detector, meant as a tool for uniform and high accuracy imaging of massive detector volumes, was based on the fact that in highly purified LAr ionization tracks could indeed be transported undistorted by a uniform electric field over distances of the order of meters [18]. Imaging is provided by wire planes placed at the end of the drift path, continuously sensing and recording the signals induced by the drifting electrons.

The feasibility of this technology was further demonstrated by the extensive ICARUS R&D program, featuring several prototypes of increasing mass. The largest of these devices had a mass of 3 tons of LAr [19, 20]. A smaller device with 50 l of LAr [21] was also exposed to the CERN neutrino beam, demonstrating the high recognition capability of the technique for neutrino interaction events.

The realization of the 600 ton ICARUS T600 detector and of its test carried out at surface [22] demonstrated that the LAr TPC technique can be operated at the kton scale with a drift length of 1.5 m. Data taking of about 30000 cosmic-ray triggers has allowed to test the detector performance in a quantitative way [23, 24, 25, 26, 27]. The success of the industrial construction of the T600 module and its excellent performance has motivated the idea of cloning the detector to reach larger mass scale, as required to accomplish astroparticle physics experiments at LNGS [28].

2 Physics framework

We can schematically summarize our present knowledge on (massive) neutrinos by stating that

- there is evidence for three light neutrinos in Nature, as an outcome of the LEP experiments [10];
- direct neutrino mass measurements have so far only yielded limits in the range of 1 eV or less. Very stringent limits have also recently come from cosmological measurements [11];
- neutrino oscillation experiments with solar and atmospheric neutrinos have contributed to build up a solid evidence for neutrino oscillations, hence confirming that neutrinos are massive: this must be considered as the first compelling evidence for physics beyond the Standard Model of particles and interactions;
- neutrino mixing is described by the so called Pontecorvo, Maki, Nakagawa, Sakata (PMNS) 3 x 3 matrix. Two of the mixing angles are rather large (θ_{12} and θ_{23}) while the third is

small. The two Δm^2 experimental values confirm the smallness of the neutrino masses (see *e.g.* [12]).

We start by briefly presenting the neutrino mixing matrix and some of its peculiar features. The unitary PMNS mixing matrix can be parameterized as

$$U(\theta_{12},\theta_{13},\theta_{23},\delta) = \begin{pmatrix} c_{12}c_{13} & s_{12}c_{13} & s_{13}e^{-i\delta} \\ -s_{12}c_{23} - c_{12}s_{13}s_{23}e^{i\delta} & c_{12}c_{23} - s_{12}s_{13}s_{23}e^{i\delta} & c_{13}s_{23} \\ s_{12}s_{23} - c_{12}s_{13}c_{23}e^{i\delta} & -c_{12}s_{23} - s_{12}s_{13}c_{23}e^{i\delta} & c_{13}c_{23} \end{pmatrix} \quad (1)$$

with $s_{ij} = \sin\theta_{ij}$ and $c_{ij} = \cos\theta_{ij}$, and with the freedom of the complex phase (physical only if $\theta_{13} \neq 0$). For the special case of $\nu_\mu \to \nu_e$ oscillations and under the empirical assumptions (justified by the experimental results) that $\Delta m^2_{atm} >> \Delta m^2_{sol}$, that L is comparable to the atmospheric oscillation length, and that the angle θ_{13} is small, the general three-neutrino oscillation formula can be developed as a sum of terms

$$\begin{aligned} P(\nu_\mu \to \nu_e) &= 4c^2_{13}s^2_{13}s^2_{23}\sin^2\Delta_{31} \\ &+8c^2_{13}s_{13}s_{23}c_{23}s_{12}c_{12}\sin\Delta_{31}\left[\cos\Delta_{32}\cos\delta - \sin\Delta_{32}\sin\delta\right]\sin\Delta_{21} \\ &-8c^2_{13}s^2_{13}s^2_{23}s^2_{12}\cos\Delta_{32}\sin\Delta_{31}\sin\Delta_{21} \\ &+4c^2_{13}s^2_{12}\left[c^2_{12}c^2_{23} + s^2_{12}s^2_{23}s^2_{13} - 2c_{12}c_{23}s_{12}s_{23}s_{13}\cos\delta\right]\sin 2\Delta_{21} \\ &-8c^2_{13}s^2_{13}s^2_{23}(1-2s^2_{13})\frac{aL}{4E_\nu}\sin\Delta_{31}\Big[\cos\Delta_{32} - \frac{\sin\Delta_{31}}{\Delta_{31}}\Big] \end{aligned} \quad (2)$$

where s_{ij}= $\sin\theta_{ij}$, c_{ij}= $\cos\theta_{ij}$, $\Delta_{jk} \equiv \Delta m^2_{jk}L/4E_\nu$ and $a = 2\sqrt{2}G_F N_e E_\nu = 1.54 \times 10^{-4} Y_e \rho(g/cm^3)E_\nu(GeV)$ with a is given in eV^2.

In the above formula the leading term is the first one. The third and fourth terms give CP conserving (small) contributions. The second term includes the CP violating effects due to sin δ. The last term includes matter effects, due to the passage of the oscillating neutrino through matter. One can notice that the θ_{13} angle is the 'link' between the atmospheric and the solar term. This term has great importance for future studies, since it determines the size of any CP violating effects.

The above relation reduces to the following one if one restricts to vacuum oscillations computed to leading order $P(\nu_\mu \to \nu_e) \approx \sin^2 2\theta_{13}s^2_{23}\sin^2\Delta_{31}$. A similar approximate expression can be derived for a ν_μ disappearance search $P(\nu_\mu \to \nu_x) \approx 1 - \cos^4\theta_{13}\sin^2 2\theta_{23}\sin^2\Delta_{31}$.

Interesting and stimulating is the list of the 'unknowns'. First is the actual neutrino mass scale and even more the explanation of why neutrino masses are small as compared to the masses of the other fermions. The second question is why (two of) the mixing angles are large (differently from what happens for the quark mixing) and why the third angle is apparently small. Another issue is the neutrino mass hierarchy: is the tau-neutrino the heaviest? Is Δm^2_{23} positive or negative? These last questions can be addressed by studying matter effects (MSW), namely the corrections to the vacuum oscillation scheme for neutrinos oscillating through matter [14]. Last but not least, there is the subject of CP violation in the neutrino sector. The PMNS matrix has a phase term that, if non zero, could cause CP violating effects, detectable *e.g.* by comparing oscillation results obtained with neutrinos and antineutrinos.

The answer to the above outstanding questions will likely keep neutrino physicists occupied for the next two decades, similarly to the time that has been required to go from the first signals of anomaly in the solar neutrino fluxes to the solid establishment of neutrino oscillations as of today.

Table 1: Global fit of oscillation data (from [12]).

Parameter	best fit value	3σ
Δm^2_{21} (10^{-5} eV^2)	7.9	7.2-9.1
Δm^2_{31} (10^{-3} eV^2)	2.3	1.4-3.3
$\sin^2\theta_{21}$	0.3	0.23-0.38
$\sin^2\theta_{23}$	0.5	0.34-0.68
$\sin^2\theta_{13}$	0.002	$<$0.047

The present scenario is summarized in Table 1, where the results of a global fit of all oscillation data are presented [12]. In this, we assume that mixing occurs among three active neutrinos (two Δm^2 and three mixing angles) and that, therefore, we do not take into account the so called LSND effect, that if real would naturally lead to the existence of a fourth (sterile) neutrino. The Fermilab MiniBoone experiment will soon clarify this issue [13].

From the above relations it turns out that a measurement of θ_{13} can be accomplished by detecting (appearance) $\nu_\mu \to \nu_e$ oscillations, where the other mixing angles can be determined with a disappearance experiment. These measurements can be well performed with accelerator neutrino experiments. However, the main experimental limitations are given by the prompt ν_e contamination in ν_μ beams, by the π_0 background capable to fake the production of electrons, and by the additional background of low energy muons and pions that can be misidentified as electrons. Obviously, the relevance of these backgrounds strongly depends upon the parameters of the neutrino beam and on the adopted detection technique.

In any case, given the smallness of the effect ($< 5\%$), the use of next generation high-intensity beam facilities is a must. In particular, one usually thinks of Super-Beams, namely conventional accelerator neutrino beams fed by high-intensity proton accelerators able to increase by factors 10-100 the presently achievable neutrino intensities. This is the case of the T2K experiment at JPARC, the first neutrino Super-Beam to be operational.

3 Motivation of a 100 ton liquid Argon TPC at 2 km

As already mentioned, the T2K LBL program foresees near stations at 140 and 280 m, an option for a second intermediate station at 2 km and the far station composed by the existing Super-Kamiokande detector. The following items will need to be addressed in order to achieve the challenging goals of T2K

- **for the disappearance experiment**: a very good knowledge of the neutrino beam will have to be reached in order to determine precisely the Δm^2_{23} and $\sin^2 2\theta_{23}$ parameters with small systematic errors;
- **for the appearance experiment**: a very good knowledge of (a) the intrinsic ν_e component of the beam and (b) the π^0 production in neutrino interactions in the GeV range will be mandatory in order to understand precisely the beam associated backgrounds to the electron appearance search;

The expected flux of the neutrino beam at the 2 km site is shown for all the neutrino flavor components in Fig. 2.

In Fig. 3 the interacting neutrinos energy spectrum is shown for each component of the beam. Table 2 summarizes the integral of the fluxes shown in Fig. 2 and also indicates the total

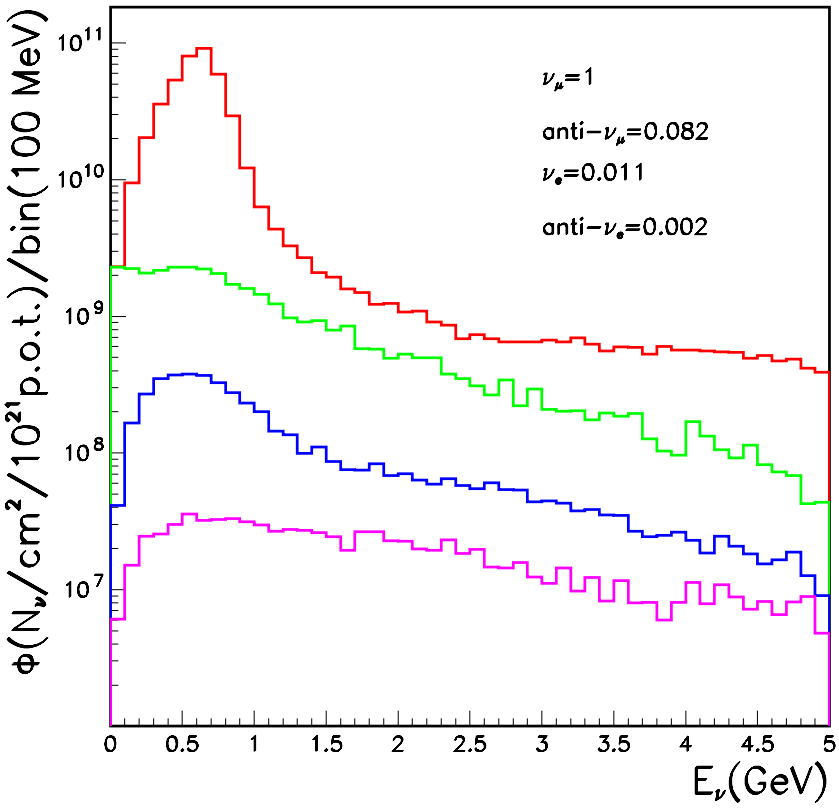

Figure 2: The neutrino beam energy spectrum expected at the 2 km site is shown for all the neutrino flavor components.

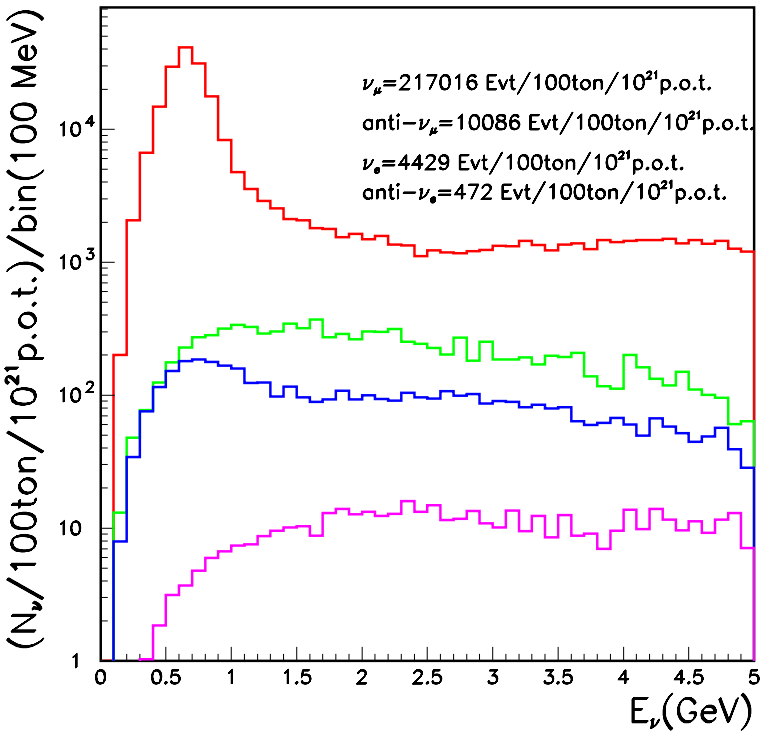

Figure 3: Energy spectra of interacting neutrinos for 100 ton of target mass and 10^{21} p.o.t..

number of neutrino interactions, according to the distribution is shown in Fig. 3. The number of interactions are refered to a detector mass of 100 ton and to 10^{21} p.o.t..

We assume that the near detectors will be composed of different technologies, like in the case of the presently running K2K experiment, that includes both a water Cerenkov (1 kton mass) and a fine-grained detector. In particular, an improved near detector (SciBar) has been recently built for K2K to upgrade the former near detector complex [30]. The main motivation has been to improve the measurement of the neutrino energy spectrum by using QE interactions. In order to select this event sample with high purity and efficiency, and in parallel to suppress other interactions such as inelastic interactions with pions, the device is designed to provide high efficiency in the detection of all charged particles produced in the interaction. One has to stress that the energy spectrum measured by the water Cerenkov detector, that is basically the (visible) energy of the outgoing muon, cannot be used to predict the oscillated spectra at the

Table 2: The integrated flux for all beam flavor components is summarized in units of $10^{10}/cm^2/10^{21}$ *p.o.t.*. The number of neutrino interactions is listed for a detector mass of 100 ton. The NC column refers only to the inelastic reactions.

			# of interactions		
Flavor	Flux	Relative Flux	CC(QE)	NC	TOT
ν_μ	43.77	1.	190763(121859)	26253	217016
$\overline{\nu}_\mu$	3.60	0.082	8023(2764)	2063	10086
ν_e	0.49	0.011	3704(1372)	725	4429
$\overline{\nu}_e$	0.09	0.002	372(96)	100	472

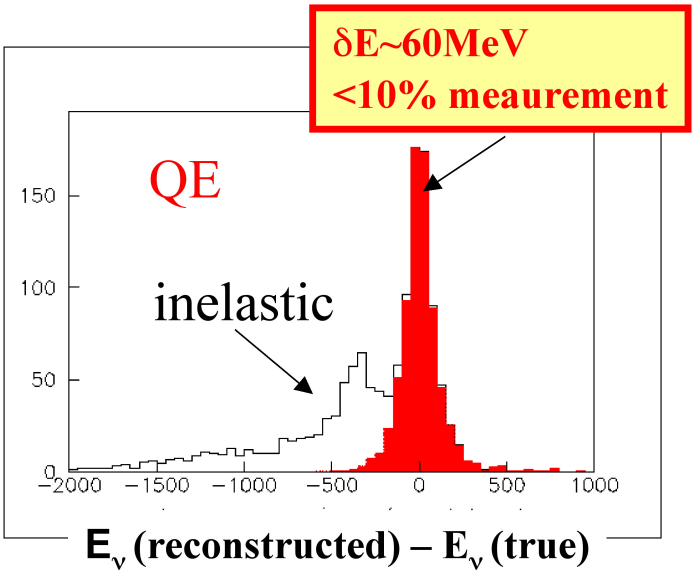

Figure 4: Simulation showing the difference between the reconstructed and the true neutrino energy in Super-Kamiokande.

Super-Kamiokande far detector, due to the lack of knowledge of all the details of the neutrino interactions, being the neutrino energy $E_\nu = E_\mu + E_{had}$ (see Fig. 4). This measurement can be accomplished by exploiting the features of the fine grained detector.

The upgraded K2K fine grained detector consists of plastic scintillator strips with fine segmentation. The scintillator itself is a neutrino target and has no dead regions. Due to the fine segmentation of the detector, short tracks down to 10 cm length can be efficiently detected. The device has also particle identification capabilities (especially for protons and pions) with dE/dx information obtained by measuring the energy deposition in each strip. The weight of the active detector target is about 15 ton. This mass will have to be accordingly scaled up with the distance in the case of the T2K 2 km site, reaching a fiducial mass of about 100 ton. The event rate would then be about 300000 events per year.

Needless to say, the extrapolation of a volume-instrumented mass such as the fine-grained scintillator detector of K2K to the T2K 2 km site would not be a practical solution. On the contrary, a surface-instrumented device like a liquid Argon TPC could be envisaged, since this technique would allow to readily reach the required mass while keeping the fine granularity. For example, the imaging of a ν_e quasi-elastic charged current event is illustrated in Figure **??**.

Concerning the physics potentialities, a 100 ton liquid Argon TPC detector at the 2 km T2K site would be in particular relevant for the

- the measurement of ν_μ CC events. The liquid Argon TPC provides an independent measurement of the off-axis flux. The excellent muon identification makes the selected sample very clean and the reconstruction will be unbiased. The low momentum detection threshold in LAr compared to water Cerenkov allows for an independent classification and measurement of event samples in the GeV region. This will provide independent systematic on the not-QE/QE ratio and on the energy scale. In addition, the independent

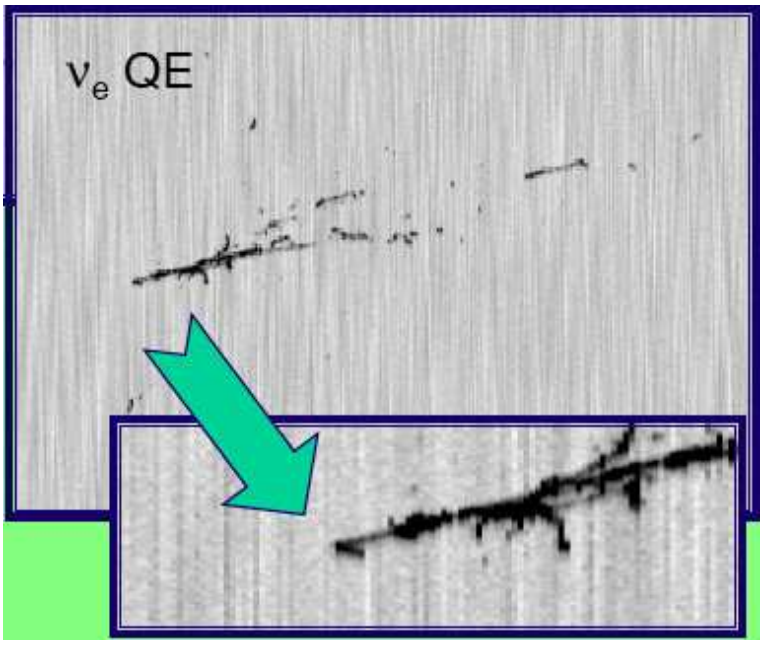

Figure 5: Imaging of a simulated ν_e quasi-elastic charged current event.

reconstruction effects in water Cerenkov can be studied with events recorded in LAr and this will help in the understanding the systematic errors in extrapolating the 1 kton water Cerenkov response to Super-Kamiokande. Finally, the energy independent detection and measurement efficiency for sub-GeV and multi-GeV events in LAr will provide a measurement of the high energy muon neutrinos from kaon decays for an extra handle on the ν_e component of the beam;

- the measurement of ν NC events. The clean measurement of the π^0 production provides an independent information on the systematic error on the NC/CC ratio. One can also address independently the coherent production by looking for the absence of tracks at the vertex. The clean e/π^0 separation available thanks to the excellent event and particle identification plays here an important role;

- the measurement of intrinsic ν_e CC events. The excellent event and particle identification gives clean e/μ and e/π^0 separation with an unbiased reconstruction. This will provide an independent measurement of the ν_e contamination, well separated from the π^0 background. Combined with the NC background, it will yield independent and separated ν_e and π^0 background components at the far detector;

- standard model neutrino interactions in the GeV region. The bubble-chamber like imaging of the LAr TPC will permit the study of neutrino interactions with high quality and, given the flux and the large mass, with high statistics. This sample of events will allow the study of the DIS+resonance modelling, the QE modelling (form factors, ...), and the nuclear effects (binding, Fermi-motion, Pauli-exclusion, NN-correlations, PDF modifications, rescattering, ...).

We recall that the neutrino beam at JPARC is constructed as an off-axis beam with an angle between 2 and 3 degrees. While a lot of experimental knowledge has been acquired with the

prediction of on-axis fluxes, there is no previous experience in the operation of off-axis beams. In particular, we note that the systematics associated to on- and off-axis beam could be quite different. In an on-axis beam, the prediction of the neutrino flux requires a good knowledge of the meson spectrum yield and to lesser extent of their angular distribution, since the beam at the far location is very wide and the detector is placed at the maximum of the flux. On the other hand, an off-axis beam requires the knowledge of the meson spectrum with less precision, since in the ideal case of the Jacobian peak the neutrino flux is actually independent of the parent meson momentum. Hence, the meson spectrum is less important. On the contrary, angular effects are most important, as can be appreciated by considering the modification in the neutrino spectrum when the beam angle is changed by 1 degree. It appears natural that a conservative approach to the first ever performed off-axis experiment with the goals of measuring very precisely the oscillation parameters will require some level of redundancy.

In the conceptual design of the proposed liquid Argon detector for the T2K 2 km station we are also considering the possibility of inserting a (iced) water or solid CO_2 inner target inside the active volume of the detector. In this way one could collect a statistically significant sample of neutrino events with interaction in Oxygen (as in Super-Kamiokande) but with the produced particles reconstructed in the liquid Argon volume, therefore exploiting the low detection threshold and the imaging capabilities of the detector.

4 Detector overview

4.1 The 2 km station complex

4.2 The liquid Argon detector and its infrastructure

The LAr TPC detector for the T2K 2 km site is hosted in a 8 m long and 7 m diameter stainless steel dewar positioned on mechanical shock absorbers, schematically shown in Fig. 9. Inside the outer dewar an inner vessel of 6 m in length and 6 m in diameter contains the liquid Argon. The volume between the two vessels is evacuated to ensure adequate thermal insulation. The inner vessel contains about 240 ton of liquid. A smaller volume of about 150 ton is confined by the inner Time Projection Chamber (TPC), corresponding to a neutrino interaction fiducial volume of about 100 ton. The chamber consists of a stainless steel mechanical frame with parallelepiped shape inscribed in the inner vessel cylinder (see Fig. 10).

The cathode of the TPC is placed in the middle of the inner volume, along the longitudinal axis. There are two options for this element, according to the choice we will make about the structure of the inner target, filled with iced water or with solid CO_2. The first option foresees a cylindrical target structure (Fig. 12) made of a 2 mm thick stainless steel cylinder of 60 cm diameter and 6 m length. In this case, the cathode is a pierced stainless steel plane placed longitudinally along the dewar main axis holding the inner target. The second option refers to a parallelepiped shaped inner target (Fig. **??**) 25 cm thick and 6 m long. In this latter case there would be two separate cathode planes placed onto the external sides of the target. In both cases, the cathode electrode defines two half-volumes. Each of the two extreme sides of the half-volumes are equipped with two or three wire planes with different wire orientation which constitute the readout anodes.

The electric field perpendicular to the wires is established in the LAr volume by means of a high voltage (HV) system in order to permit and guide the drift of the ionization electrons. The system is composed of the above mentioned cathode plane, parallel to the wire planes, placed in the center of the cryostat volume at a distance of 1.8 m from the wires of each side, hence defining the maximum drift path. The HV system includes field shaping electrodes required

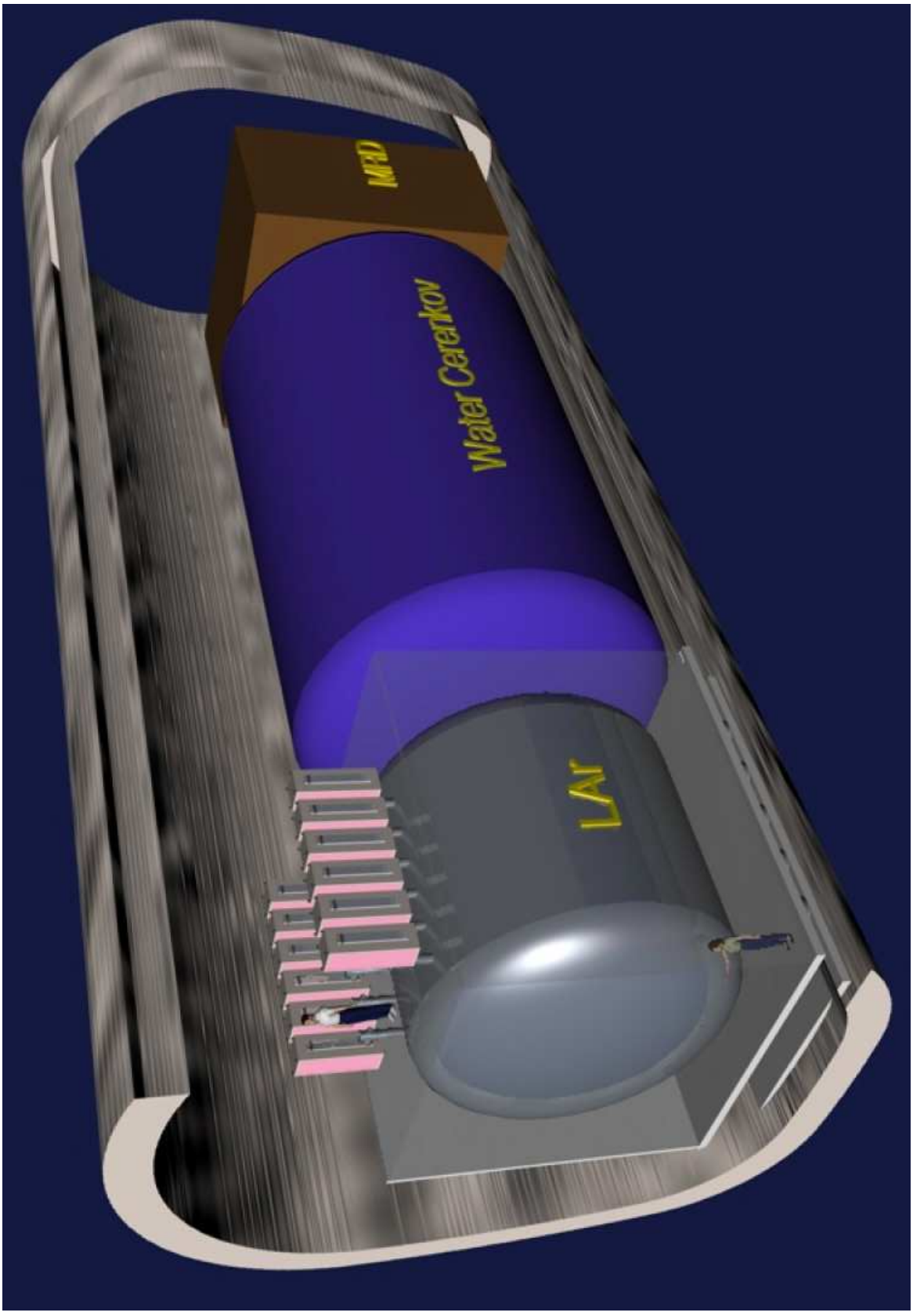

Figure 6: Artistic view of the proposed 2km complex.

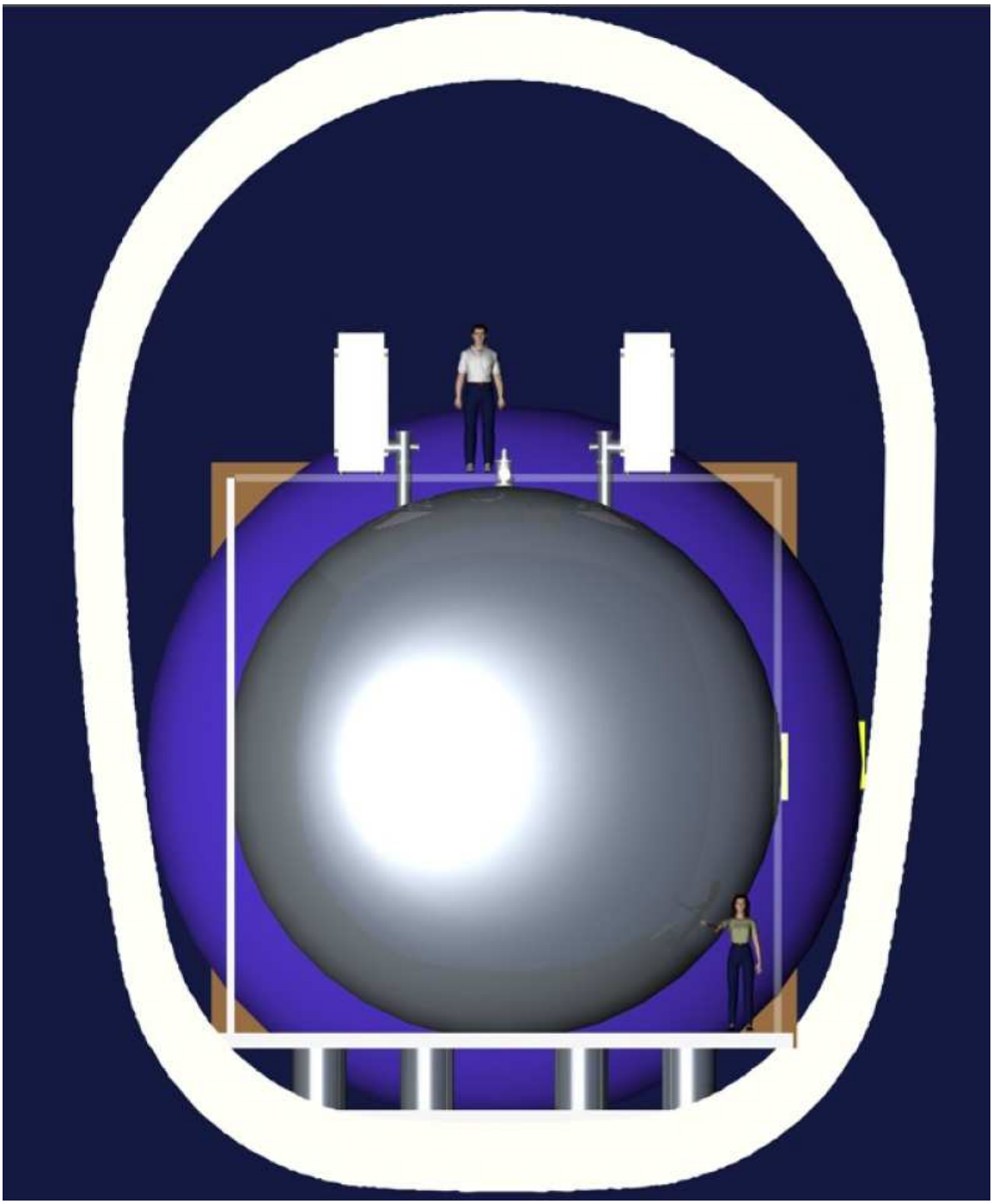

Figure 7: Front view of the proposed 2km complex.

Figure 8: Side view of the proposed 2km complex.

to guarantee the uniformity of the field along the drift direction and a HV feedthrough to set the required potential on the cathode. At the nominal voltage of 210 kV, corresponding to an electric field of 1 kV/cm, the maximum drift time in LAr is about 1 ms.

Large surface photomultipliers (PMTs) are placed inside the liquid, attached to the supporting mechanical structure, outside the inner fiducial volume.

On top of the cryostat there are flanges equipped with cryogenic feedthroughs for the electrical connection of the wires with the read-out electronics, and for the internal instrumentation including PMTs, purity monitors, level meters, temperature probes, etc. The electronics allow for continuous read-out, digitization and wave-form recording of the signals from each wire of the TPC. The front-end electronics is host in 12 crates directly placed on top of the dewar.

The passage of charged particles inside the LAr volume produces both ionization and scintillation light signals. Detection of this light by the PMTs provides a method for the absolute time measurement of the event and an internal trigger signal. Reconstruction of ionizing tracks is performed by using charge and the light signals. Ionization electrons induce detectable signals on the TPC wires during their drift towards and across the wire planes while and UV photons from scintillation provide a prompt signal on the PMTs that allows the measurement of the absolute drift time and, hence, of the distance traveled by the drifting electrons. In this way, each of the planes of the TPC provides a two-dimensional projection of the event image, with one coordinate given by the wire position and the other by the drift distance. A 3D reconstruction of the event is obtained by combining the information from wire planes occurring at the same drift distance.

Some of the PMTs may also optimized for the detection of Cerenkov light produced in LAr, a process that has been studied by the ICARUS Collaboration [31]. This feature may provide additional handles to improve the quality of the event reconstruction. **AR, I WOULD REMOVE THE ABOVE PARAGRAPH IN ABSENCE OF QUANTITATIVE STUDIES**.

We finally observe that the events occurring in the inner water (CO_2) target are reconstructed by the detection of particle tracks escaping from the target into the external (instrumented)

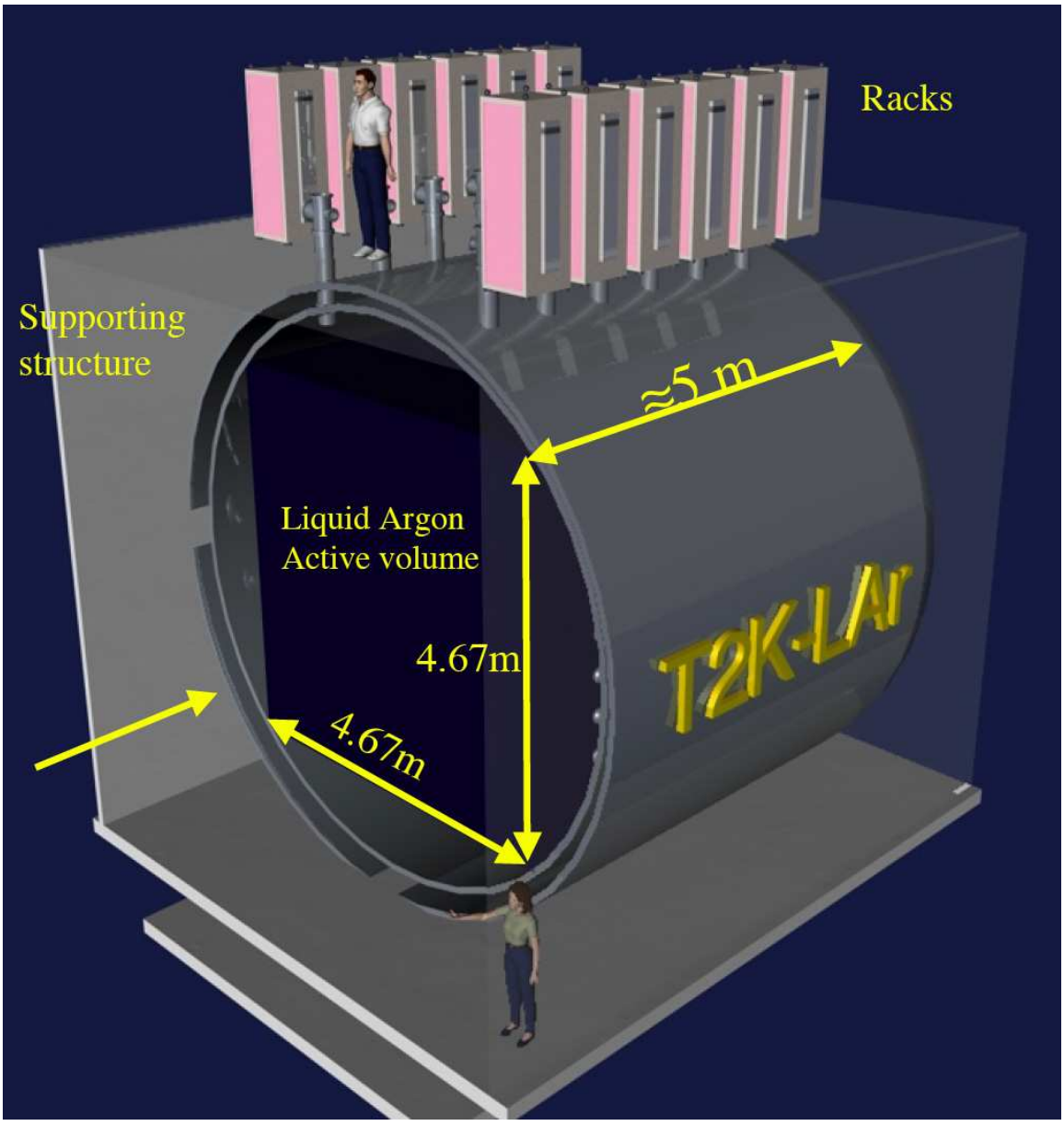

Figure 9: Artistic view of the proposed 100 ton liquid Argon TPC detector (upstream endcap removed).

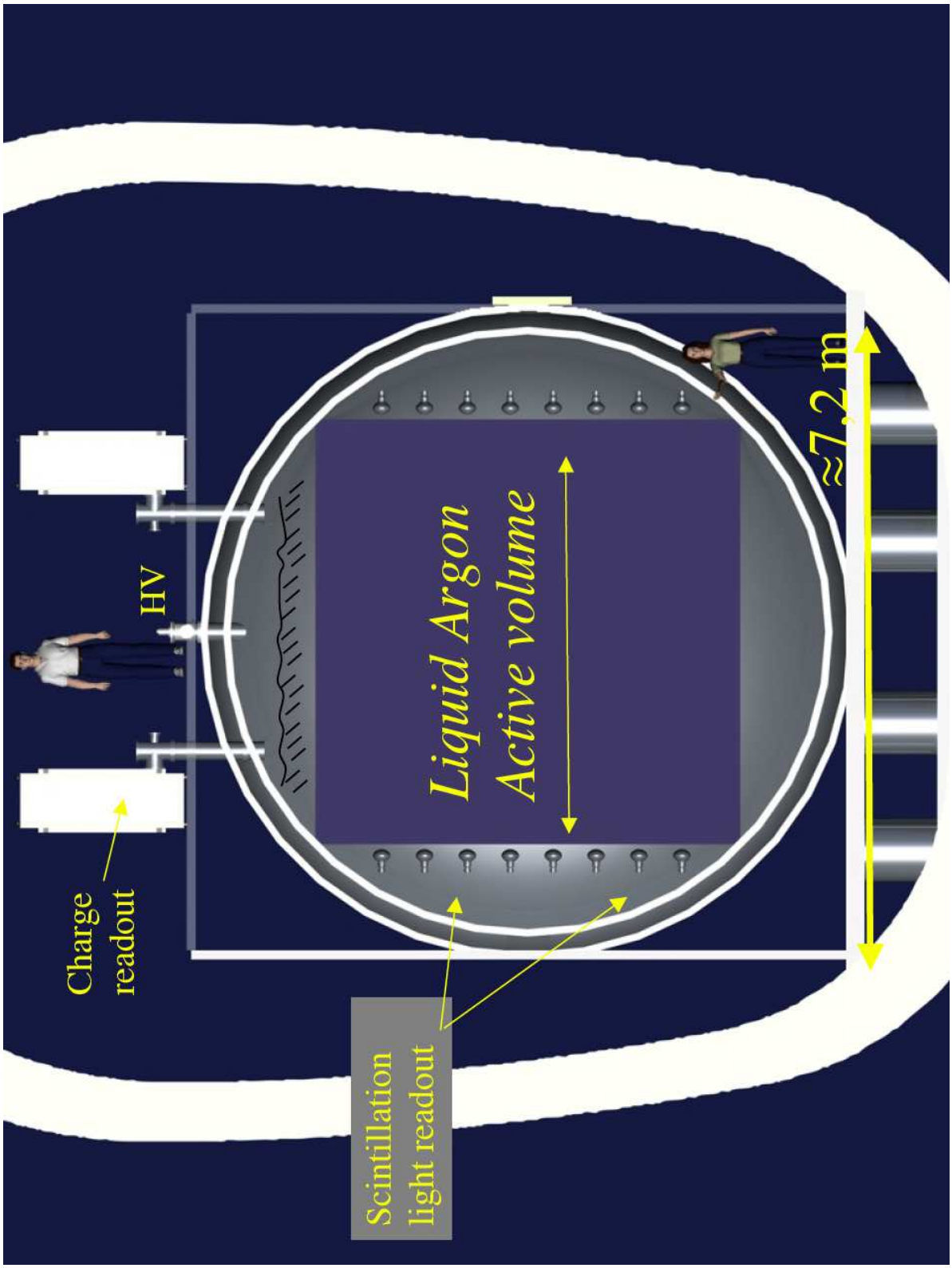

Figure 10: View of the inner layout of the TPC detector.

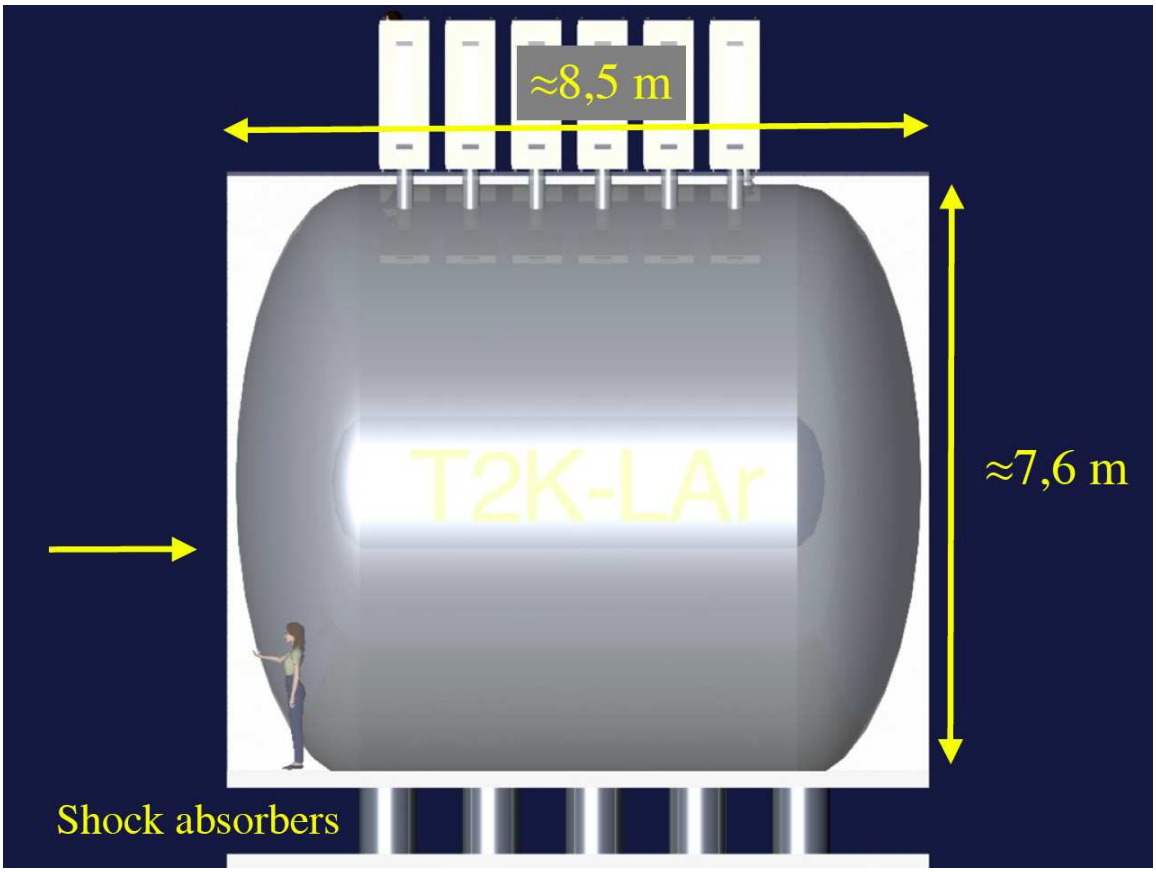

Figure 11: Side view of the TPC detector.

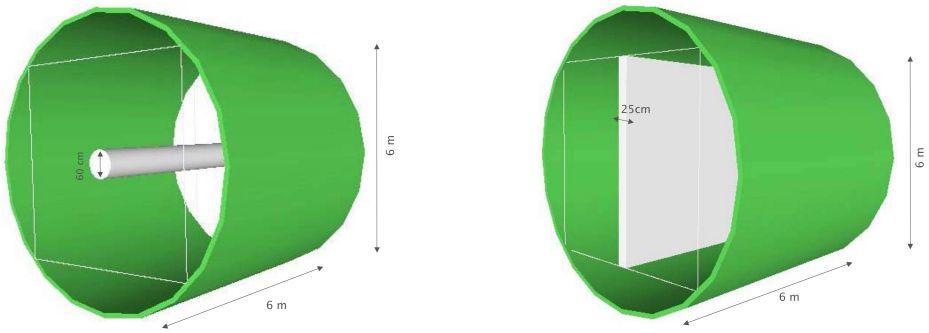

Figure 12: The inner dewar volume with (left) the option of a cylindrical inner target. (right) the option of a parallelepiped shaped inner target **FIGURES TO BE REDONE WITH RIGHT DIAMETER**.

liquid Argon TPC volume.

The detector is complemented by ancillary cryogenics systems. A gas and liquid recirculation and purification system, a heat exchanger and a LAr buffer are placed in the underground cavern, close to the detector dewar. These equipments are connected through cryogenic pipes to surface, where Argon storage, compressor, ventilation and evaporation systems complete the detector infrastructure.

5 The liquid Argon cryostat

5.1 The cryostat

The basic concept for the liquid Argon cryostat has been developed and engineered. We followed the internationally recognized codes for the design of conventional cryogenic-fluid pressure storage-vessels as covered in the ASME (American Standards of Mechanical Engineers) Boiler & Pressure Vessel Code, Sect. VIII (www.asme.org). Design and construction according to these standards should ensure a reliable and safe operation.

The cryostat consists of two concentrically mounted stainless steel cylinders with D-shaped end caps (see Figure 14). The inner cylinder contains the purified liquid argon with the drift chamber and will be wrapped with layers of superinsulation; the outer cylinder acts as a thin "skin" for vacuum insulation.

The total weight of the inner cylinder filled with liquid argon and the drift chamber is supported from the ground (at room temperature) so that the outer cylinder is only a shell without any mechanical support function. There are a total of XXX stands foreseen, (see Figure XXX). The supports have to be vacuum insulated between the inner and the outer cylinder and provide good thermal insulation between the inner cylinder at LAr temperature (about 89 K) and the ground at room temperature. This is achieved by using ceramics to support the weight and long connections between the warm and cold parts; Figure 15 shows a cut view of a support. One of the supports in the center is fixed, the others can slide in the longitudinal and/or transverse direction to accommodate the thermal contraction of the inner vessel during the cooling down.

Detailed finite element calculations have been performed (see Figure 17) to optimize the wall thickness, the positions and strength of the reinforcing rings and the supports, and to make sure that the ASME Pressure Vessels specifications for these tanks are fulfilled.

There are feedthrough flanges on the inner and on the outer cylinder, i.e., the cables and filling tubes are lead through the insulation vacuum from the cold inner cylinder to the outer cylinder at room temperature. Pumping ports are foreseen to pump the inner cylinder before it is filled with LAr and for the outer cylinder to maintain a good insulation vacuum. An additional flange is mounted at the bottom of the dewar and can be used to drain the dewar from LAr.

There is no active cooling foreseen of the dewar itself, e.g. with LN_2, the cooling is provided either by compensation of the boil-off or preferably via a standard Linde-Hampson refrigeration system (see Section 6.2).

5.2 The inner target

It is to be expected that the knowledge of the neutrino cross-sections and nuclear effects will improve in the coming years thanks to new measurements performed for example in K2K, Minerva, etc. However, the extrapolation between Argon and Water targets might be plagued by uncertainties, which could affect the goal of precision measurement at T2K. The "straightforward" solution is to insert an additional target within the 100 ton liquid Argon detector.

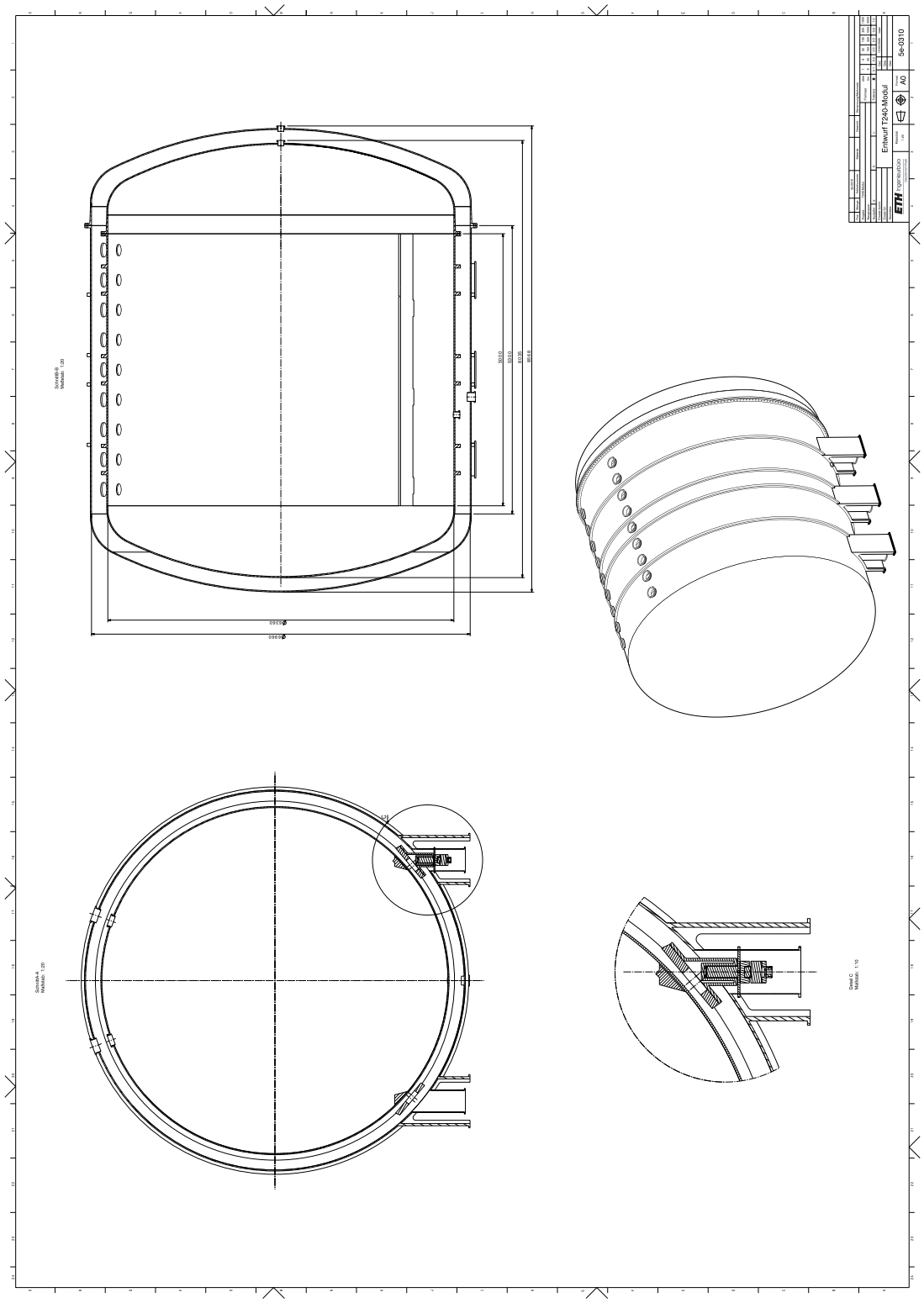

Figure 13: Drawing of the cryostat.

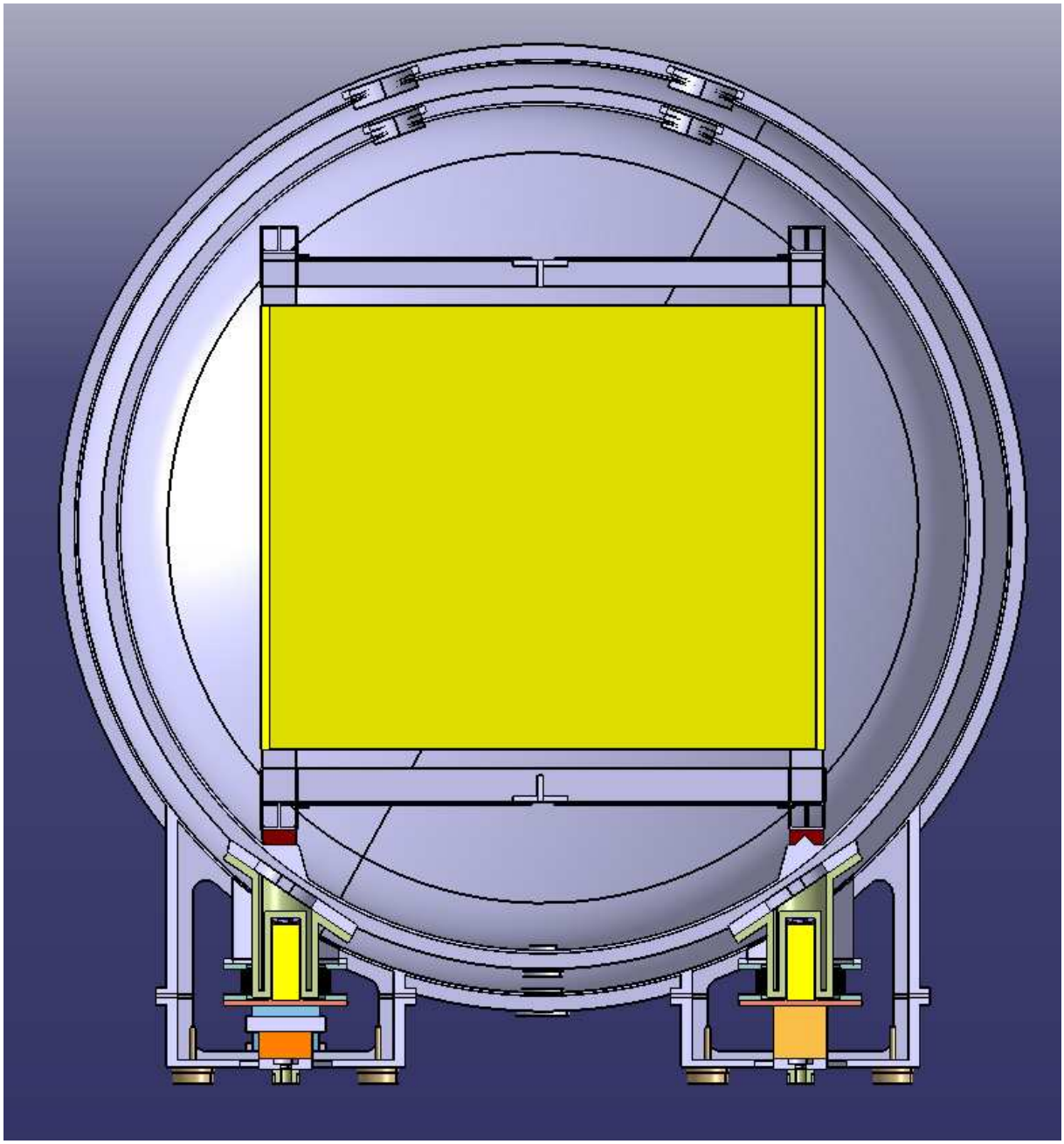

Figure 14: Cut through the LAr cryostat with the detector frame mounted inside.

Table 3: Geometrical characteristics of the cryostat.

Number of independent cylinders	2
Outer vessel	
outer diameter	7.2 m
length of cylinder	5.3 m
total length (incl. end caps)	8.5 m
axial length of screwed end cap	1.8 m
axial length of welded end cap	1.4 m
wall thickness	20 mm
weight of cylinder (incl. supports)	24 t
weight of screwed end cap	9.8 t
weight of welded end cap	7.6 t
Inner vessel	
outer diameter	6.6 m
length of cylinder	5 m
total length (incl. end caps)	8 m
axial length of screwed end cap	1.7 m
axial length of welded end cap	1.3 m
wall thickness	20 mm
weight of cylinder (incl. supports)	25 t
weight of screwed end cap	8.5 t
weight of welded end cap	6.6 t
Material of vessels	stainless steel
Thermal Insulation	multi-layer super–insulation in vacuum
Total (cold) internal volume	237 m^3
Total LAr mass	315 t

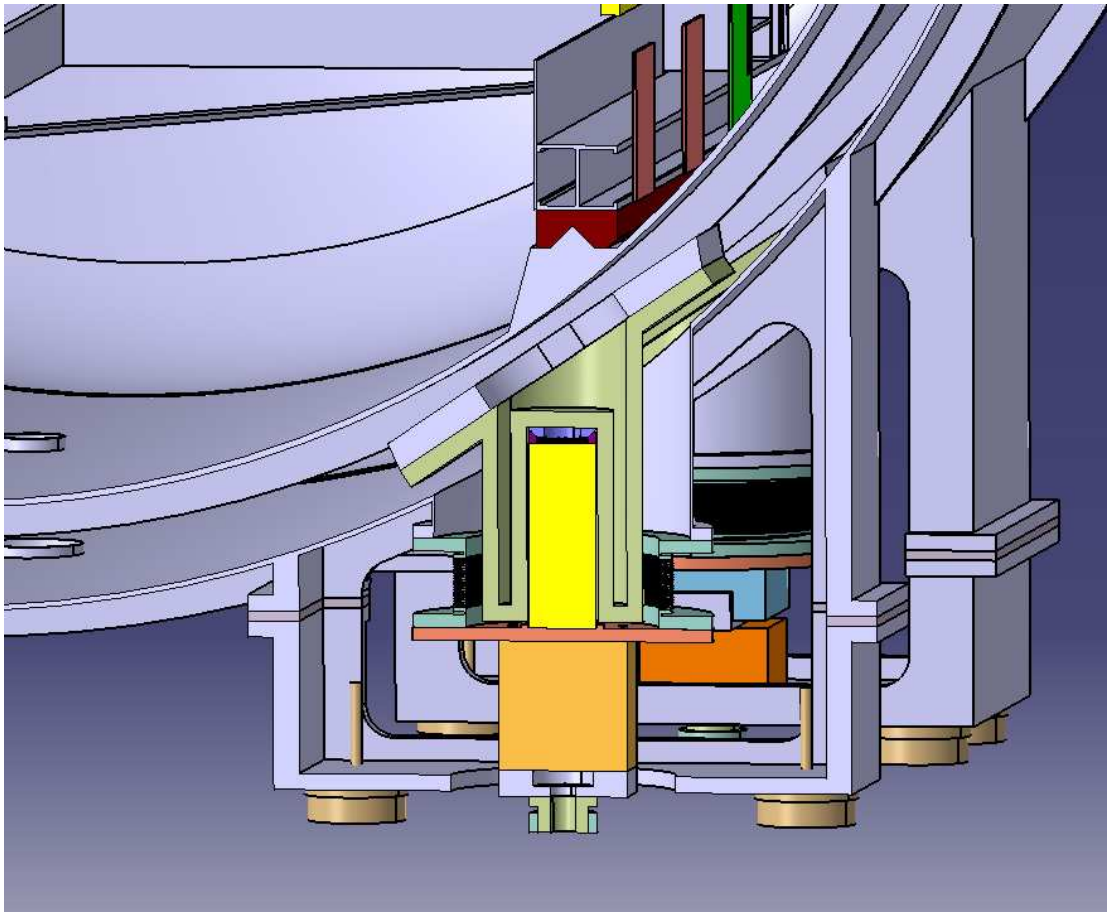

Figure 15: Cut through a support of the LAr cryostat.

This approach ("inner target" or "embedded target") is supported by kinematics of the events: indeed, at low neutrino energy secondary particles are produced at low momentum and large angles, hence one is forced to consider a target fully immersed into the liquid Argon imaging volume, and it is difficult to envision a non-immersed or upstream target, whose products would be measured in the liquid Argon with high efficiency.

The main motivation of the inner target is therefore to collect a sample of neutrino interactions with Water or Oxygen nuclei, analogous to those occurring in the far Super-Kamiokande detector, but with the particle tracks entering the liquid Argon imaging volume. One could therefore reconstruct in detail these events by exploiting the low threshold of the TPC detector and its ability in reconstructing multi prong events.

One can consider different media for the additional target (See Table 4). Most promising media are Water (H_2O) or Dry Ice (CO_2). Other elements like pure Oxygen, Nitrogen, or hydrocarbures are not favored.

The additional target medium must not enter into contact with the pure argon, otherwise contamination is possible. We assume that the additional medium is contained into a specially located volume. At this stage we consider two possibilities: (1) a specially located steel tube in the middle of the detector volume (2) a double-cathode structure whose inner volume is filled with the additional medium. The volume will be evacuated and filled during or after the liquid Argon filling phase.

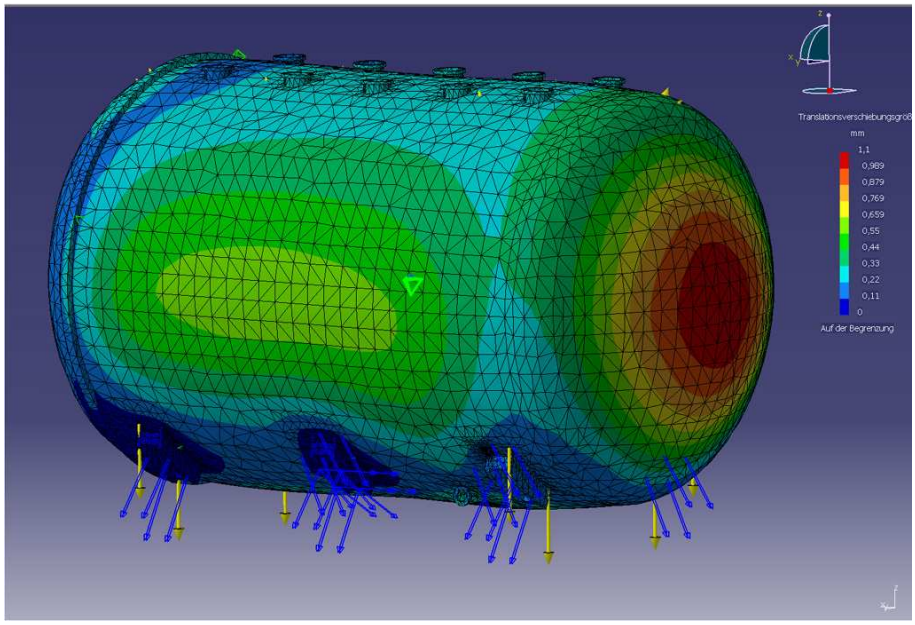

Figure 16: Results from the finite element analysis of the cryostat design: displacement map

The inner target geometry has been studied by means of simulations.....

...In Fig. 5.2(left) one can see the effect of the inner cylindrical target to the electric field lines of the detector, while Fig. 5.2(right) shows that with a parallelepiped shaped target there are no field distortions.

5.3 Flanges and services

5.4 Cryogenic infrastructure

5.5 Design of a 50 ton prototype

In order to potentially test all cryogenic and mechanical aspects, a 50 ton prototype LAr TPC was designed. It consists of two concentrically mounted stainless steel cylinders with D-shaped end caps (see Figure 19). Like for the final cryostat, detailed finite element calculations have been performed to optimize the wall thickness, the positions and strength of the reinforcing rings and the supports, and to make sure that the ASME (American Standards of Mechanical Engineers) specifications for these vessels are fulfilled.

The inner cylinder has a length (without end caps) of 400 cm and a total length of 558 cm, an inner diameter of 320 cm and a wall thickness of 1 cm; four reinforcing rings with a height of 6 cm and a width of 4 cm are distributed over the cylinder with a largest distance of 100 cm from each other. The outer cylinder has a length (without end caps) of 430 cm and a total length of 603 cm, the inner diameter is 352 cm and the wall thick thickness is also 1 cm, it is also reinforced with four rings. The two end caps on the front side can be dismounted; they are screwed to the flange on the cylinders and sealed with helicoflex sealings.

The total weight of the inner cylinder filled with liquid argon and the drift chamber is about 63 tons. This weight is supported from the ground (at room temperature) so that the outer cylinder is only a shell without any mechanical support function. There are a total of six stands foreseen, (three on both sides, see Figure 19).

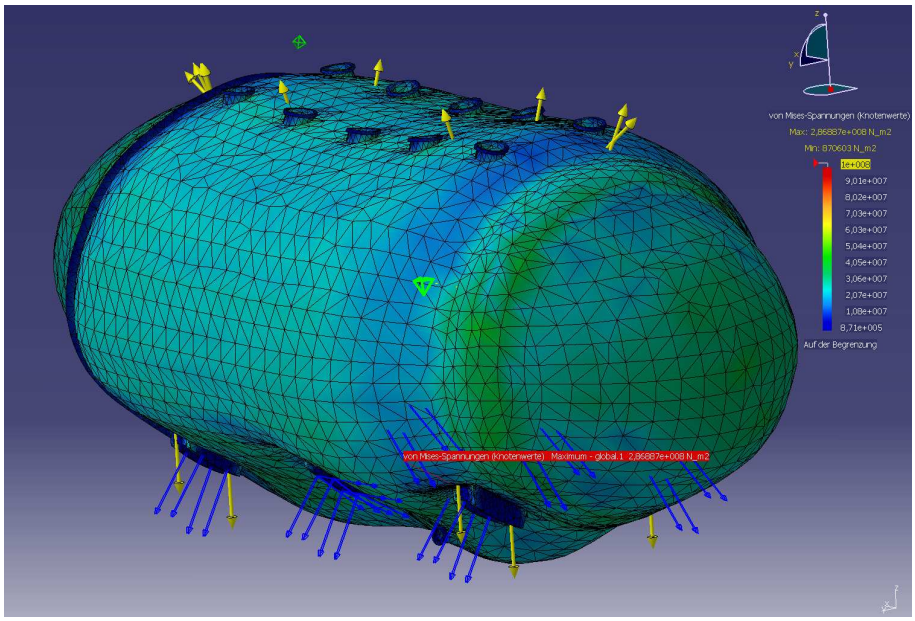

Figure 17: Results from the finite element analysis of the cryostat design: tension map

On top of the cryostat are ten CF250 flanges with the feedthroughs for the signal cables and the high voltage (about 100 kV) for the drift chamber, the cables for the slow control devices (PT10000 resistors for the temperature measurement, capacitive LAr level meters and purity monitors), and for the LAr filling and recirculation. In the center of the end caps on the front side is a flange mounted in order to be able to mount windows for tests of the detector in a beam.

6 Liquid Argon process

6.1 General features

In liquid Argon the production of free electrons and scintillation light emission are the two processes that allow its use as an active detection medium. The average energy to produce an electron-ion pair is W_{ion} = 23.6 eV; the energy needed to emit a scintillation photon is W_{ph} = 19.5 eV. The two processes are complementary and their relative strength depends on the intensity of the electric field applied to the active LAr volume. Ionization yield rises with the field value while the scintillation yield decreases. In both cases saturation occurs for field values higher than $\sim$ 10 kV/cm. At the nominal value of 500 V/cm the two processes are competing. The charge collection and imaging is performed by the TPC wire planes biased at suitable voltage. The first is affected by electron-ion recombination processes. The scintillation emission in LAr consists of VUV-light (around 128 nm) produced as radiative decay of excited molecules produced by ionizing radiation, which emit ultra-violet photons in transitions from the lowest excited molecular state to the dissociative ground state.

The main physical, chemical and thermal properties of liquid Argon are summarized in Table 6 and Table 7.

Table 4: Comparison of different nuclear targets. The mass is given for a tube of radius 30 cm.

Element	Z/A	Density (g/cm^3) Mass (ton)	X_0 (cm)	Properties	Comments
H_2O	0.555	1 1.7 ton	36.1	Freezes at 0 C	Expands when freezes
O_2	0.500	1.141 2 ton	30.0	Boiling T at 1 atm : 90.2 K	Corrosive and dangerous
N_2	0.500	0.807 1.4 ton	47.1	Boiling T at 1 atm : 77.4 K	Must be pressurized to $\approx$ 3 bar
CO_2 solid	0.500	1.56 2.7 ton	23.2	Sublimation at 186 K	Dry ice, compatible with SS
CH_4	0.623	0.42 0.7 ton	109	Boiling T at 1 atm : 112 K	Good for free protons, flammable
C_2H_6	0.599	0.51 0.9 ton	89	Boiling T at 1 atm : 184.5 K	Like CH_4

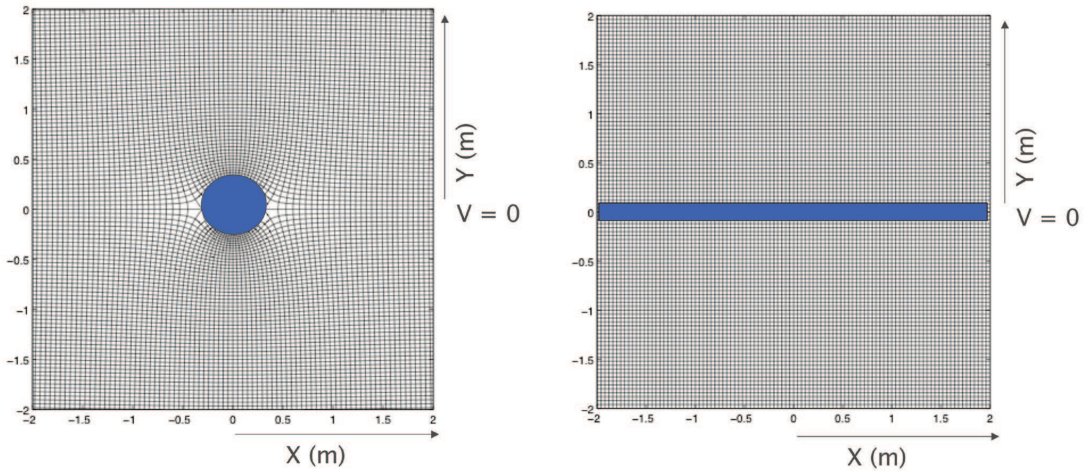

Figure 18: (left) LAr TPC electric field lines distortion induced by an inner cylindrical target. (right) Electric field lines with a parallelepiped shaped inner target.

Table 5: Geometrical characteristics of the 50 ton prototype.

Number of independent cylinders	2
Outer vessel	
outer diameter	3.54 m
length of cylinder	4.3 m
total length (incl. end caps)	6 m
wall thickness	8 mm
weight of cylinder (incl. supports)	5.3 t
total weight of end caps	2.4 t
Inner vessel	
outer diameter	3.22 m
length of cylinder	4 m
total length (incl. end caps)	5.5 m
wall thickness	10 mm
weight of cylinder (incl. supports)	5.5 t
total weight of end caps	2 t
Material of vessels	stainless steel
Thermal Insulation	multi-layer super–insulation in vacuum
Total (cold) internal volume	41 m^3
Total LAr mass	54 t

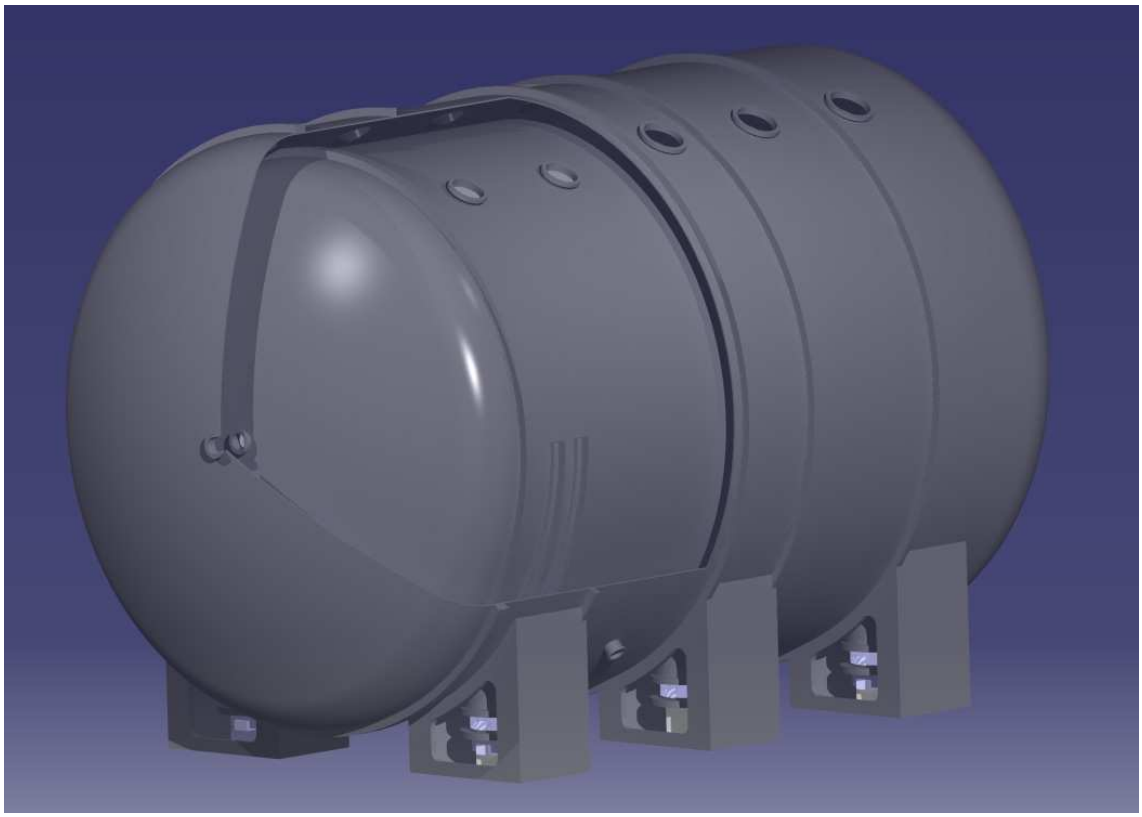

Figure 19: Cut view of the 50 ton prototype of the cryostat.

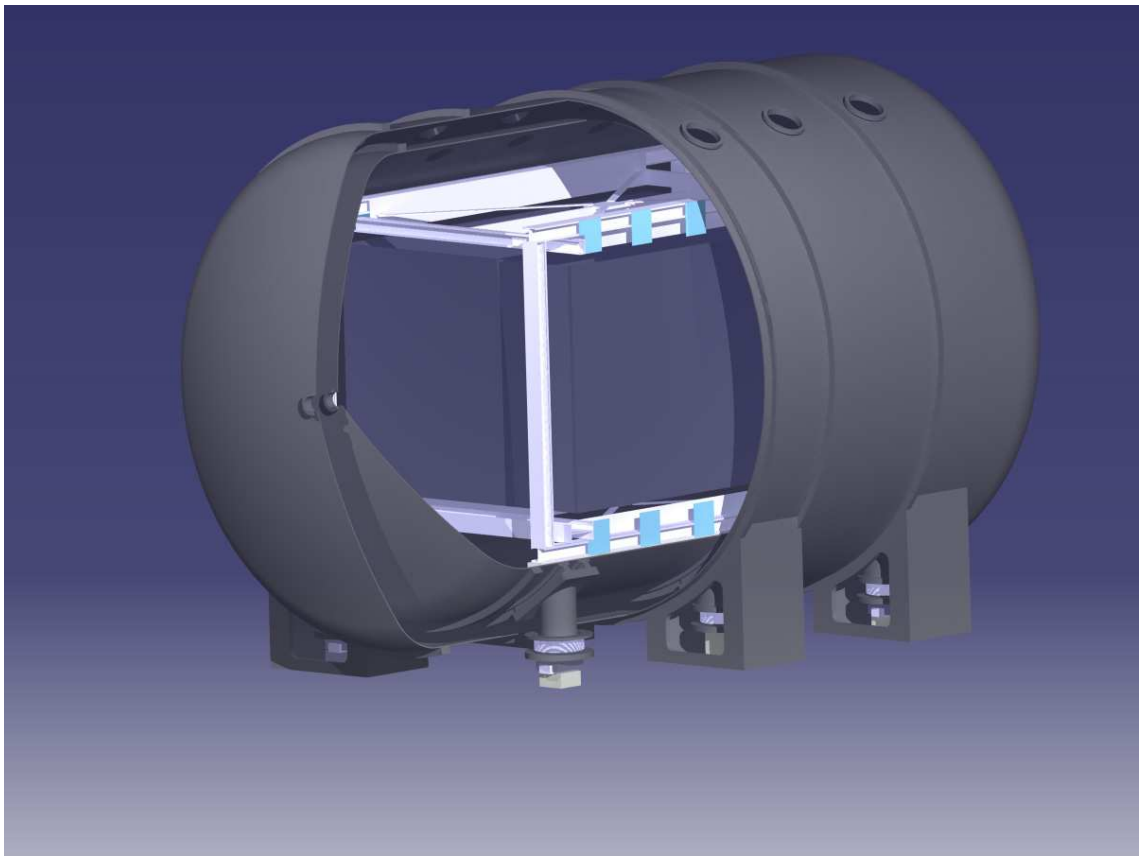

Figure 20: Open view of the 50 ton prototype of the cryostat.

Table 6: Liquid Argon properties (I).

Atomic number, mass	18, 40
Atomic weight	39.948 m_u
$\langle Z/A \rangle$	0.45059
Concentration in air	0.934 %
W_{ion} (1 MeV e^-)	23.6 eV
Energy loss $\langle dE/dx \rangle$ (minimum ionizing particle)	1.519 MeV cm^2/g
Critical energy (electrons)	31.7 MeV
W_{ph} (1 MeV e^-)	19.5 eV
Photon yield - scintillation - (@ 128 nm) [0-field]	$\sim 4.0\times 10^4$ ph/MeV
Decay time constants (for mip)	$\sim$ 6 ns (23%), $\sim$ 1.6 μs (77%)
Radiation length	19.55 g/cm^2
Molière radius	12.95 g/cm^2
Nuclear interaction length	117.2 g/cm^2
Max breakdown strength (depending on purity level)	1.1 – 1.4 MV/cm
Dielectric constant	1.5
Refractive index @ 128 nm (550 nm)	1.38 (1.23)
Rayleigh scattering length @ 128 nm (550 nm)	0.9 m (10^3 m)

6.2 Initial cooling and refrigeration

There is no active cooling foreseen of the dewar itself, e.g. with LN_2, the cooling is provided either by compensation of the boil-off or preferably via a standard Linde-Hampson refrigeration process (see Figure 21).

In the latter case, the argon itself is used as medium of the heat machine. In an ideal situation, the thermodynamical cycle is the following: the argon gas is compressed reversibly and isothermally from ambient conditions to some high pressure. This high pressure is selected so that the has will become saturated liquid upon reversible isentropic expansion through an expander. The final condition is taken at the same pressure as the initial pressure. In practice, high pressure argon is liquefied via a Joule-Thompson expansion valve, which for zero heat transfer (insulated valve) and zero work implies conservation of enthalpy. An ideal gas would not experience a temperature change upon expansion through an expansion valve. To our gratification, argon is imperfect at low enough temperatures and high enough pressures. During the cycle, the gaseous argon is passed through a purification filter before it is filled back as LAr to the main tank. Additional argon purification is also provided by a recirculation system through purification cartridges in liquid phase.

Refrigeration of the liquid Argon volume will be performed by means of a closed circuit with a compressor placed at surface, operated by a feed-back on the temperature and pressure of the inner vessel. Heat losses under normal operating conditions amount to about 100 l of liquid Argon per day. This corresponds to 300 W (cold) and to 6 kW of electric power. If we include the power required for the liquid Argon recirculation/purification described in the next Section one arrives at a total of 30 kW of electric power to be supplied. The refrigeration system is schematically shown in Fig. 22.

Table 7: Liquid Argon properties (II).

Heat capacity (Cp)			10.05 cal/mol K
Thermal conductivity			$3.\times 10^{-4}$ cal/s cm K
Latent heat of vaporization at boiling point			1535 cal/mol
Gas/liquid ratio (1 atm, 15^o/BPT)			835 vol/vol
	Pressure	Temperature	Density
Triple point:	0.68 bar	83.8 K	1.14 g/cm^3
Solid phase:		84.1 K	
Liquid phase:	1.00 bar	87.2 K	1.396 g/cm^3
Boiling point (@ 1 atm =)	1.013 bar	87.3 K	1.395 g/cm^3
	1.15 bar	88.5 K	1.388 g/cm^3
	1.20 bar	88.9 K	1.385 g/cm^3
	1.25 bar	89.3 K	1.383 g/cm^3
e^- Mobility (at boiling point)			500 cm^2/V s
e^- Drift velocity (500 V/cm - nominal field, 89 K)			1.55 mm/μs
e^- Diffusion coefficient (500 V/cm, 89 K)			4. cm^2/s
e^-– O_2 Trapping rate (500 V/cm, 89 K)			$\sim 7.\times 10^{10}$ l/mol s

6.3 Vacuum and liquid Argon purification

The maximum electron drift length for the proposed TPC detector is about 2 m. This implies that, for a correct operation of the detector and in order to reach a sufficiently high value for the drifting electron lifetime (a few ms), liquid Argon has to be pure with a concentration of electronegative impurities lower than 0.1 part per 10^9 (ppb) O_2 equivalent during all phases of the detector operation. This can be firstly achieved by using suitable materials, cleaning, and careful design of the internal components, as well as vacuum conditioning of the internal surfaces, since pollution of the LAr is mainly due to out-gassing of the inner surfaces in contact with the gaseous Argon.

The second requirement is that filling of the detector dewar from the external storage must be

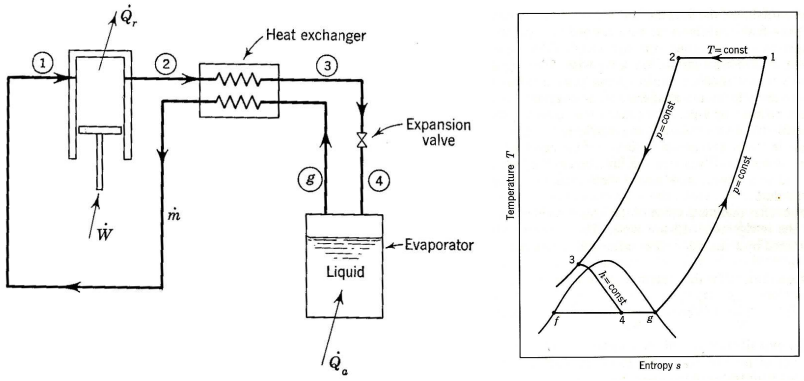

Figure 21: (left) Linde-Hampson refrigerator (right) Corresponding thermodynamic cycle.

Figure 22: Scheme of the refrigeration system.

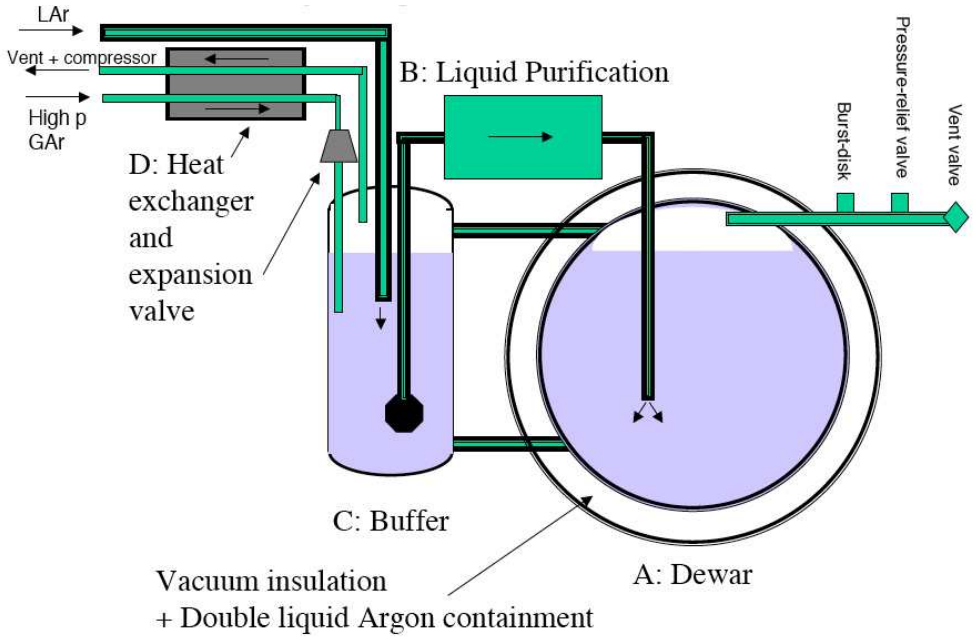

Figure 23: Scheme of the LAr cooling and recirculation system.

performed through xxx sets of Oxysorb-Hydrosorb filters[3] placed in series. Each unit is made of four identical cartridges in parallel and filled for 1/3 with Hydrosorb and for 2/3 with Oxysorb. Each set of filters is dimensioned to allow for the purification of the LAr volume starting from standard commercial LAr (with a concentration of H_2O and O_2 of about 0.5 ppm).

The third requirement is that a recirculation system has to be implemented in order to reach the ultimate purity of the liquid at equilibrium during the detector operation compensating for the external sources of impurities. We envisage, in parallel to a gas phase recirculation and purification system, the adoption of a liquid Argon recirculation. This system can be dimensioned under the requirement of a 48 hours recirculation period. This implies a recirculation rate about 3500 LAr l/hour, which corresponds to 1 l/s. This can be handled by employing 7-8 Oxysorb cartridges possibly arranged in two parallel circuits. The scheme of the liquid Argon recirculation system is shown in Fig. 23.

The operation of the system schematically consists of three logic steps. At first, vacuum is made inside the dewar at the level of (or lower than) 10^{-4} mbar. This procedure lasts about one week and allows to evacuate water, air and any other residual from the inner detector volume. In addition, one could test vacuum tightness of the detector, needed for stable and efficient operation.

The initial cooling and filling with liquid Argon follows and also lasts for about one week. This is needed to cool-down the inner-vessel and the inner instrumentation, for a total steel

[3]Hydrosorb and Oxysorb are registered trademarks of Messers-Greisheim.

Table 8: Parameters of the liquid Argon purification process.

Number of independent circuits	2
LAr Volume recirculation time	48 hours
LAr recirculation rate	3500 LAr/hr 1 LAr l/s
Purification method	Commercial Oxysorb
Typ. number of cartridges needed	8

mass of about 20 ton. This procedure should proceed quite rapidly in order to limit the amount of degassed impurities from dewar walls and inner detector components. Once the detector is cold, the level of liquid Argon can be increased and the actual filling could start.

At this point, the continuous recirculation begins. It will take nearly one month to reach the required high-purity level, that slowly improves with time. The slope of the improvement increases as the outgassing decreases with time. The asymptotic level of purity is finally reached when the speed of recirculation balances the potential rate of input of impurities, which should be zero in the ideal case. We observe that the liquid Argon phase recirculation should be minimized in order to reduce the heat input due to viscosity, to the pump operation, etc.

7 Liquid Argon monitoring

7.1 Liquid Argon purity monitors

The so-called purity monitors were first developed by the ICARUS Collaboration and have been extensively used in the various ICARUS detector prototypes, in particular for the large T600 detector [22]. Due to the vast experience gathered so far by the ICARUS Collaboration, we only give here a very general description of the device, referring to [22] and references therein for more details.

The purity monitor consists of a double-gridded drift chamber of small dimensions immersed in the LAr volume outside the fiducial imaging volume. Electrons can be extracted from a cathode via photoelectric effect. The electrons then move towards the anode following the electric field lines through a drift region between two parallel, transparent grids. During the drift path, attachment to impurities may take place, hence reducing the amount of charge collected to the anode as compared with the extracted charge. This charge ratio is a function of the electron lifetime in LAr that can therefore be estimated. The electron lifetime is directly related, by an inverse linear relationship, to the impurity concentration $N(O_2)$, namely the total concentration of impurities equivalent to Oxygen. The lifetime estimate thus provides a direct measurement of the LAr impurity content.

A possible technical implementation of a purity monitor unit is shown in Fig. 24. The purity monitor drift chamber consists of four parallel, coaxial electrodes: the photo-cathode disk K, a first grid GK at short distance from the cathode, a second grid GA facing the anode and the anode disk A at short distance from GA. A field-shaping system is formed by an array of 15 coaxial rings between GK and GA. All the elements are made of stainless steel. The two grids are Nikel meshes with 1.9 mm wire spacing, 100 μm wire diameter and nearly 90% geometrical transparency. A mechanical structure formed by a system of vetronite threaded rods, spacers and bolts, holds together the electrodes. Both materials, stainless steel and vetronite, have similar thermal coefficient to guarantee negligible thermal stresses during cooling down operations. High

Figure 24: Layout of the purity monitor and read-out scheme.

voltage potential is applied by suitable feedthroughs independently to the K, GA, A electrodes, with GK referred to ground.

The two grids and the field-shaping rings are connected by a resistor chain in order to realize a resistive divider for the electric potential applied between the two grids. The grid geometry combined with the HV bias applied to the electrodes guarantees maximum transparency, namely the minimum number of drifting electrons lost crossing a grid and maximum shielding, since the drift of the electrons before a grid does not affect the field after the grid. Each purity monitor is contained in a stainless steel, pierced Faraday cage to isolate the system from the outside electrostatic interference.

The photo-cathode is the main component of the purity monitor, since the precision on the lifetime determination depends on the actual signal-to-noise ratio provided by the system, the signal being the charge amplitude extracted from the cathode and subsequently collected by the anode. The photo-cathode material can be GaAs, Cd(Zn)Te or Au. A quartz optical fiber all silica drives the light from the source (down to 180 nm of wavelength) onto the photo-cathode. The UV light source can be a pulsed Xenon flash-lamp. The pulse width is of few μs with wavelength spectrum ranging from $\lambda \sim 185$ nm to ~ 2000 nm. The emission peak is centred around $\lambda \sim 240$ nm (~ 4.9 eV).

The photo-extracted electrons drift towards the first grid inducing a current on the cathode during a time interval t_1. After crossing GK, the electron bunch drifts along the distance between the grids. During this time (t_2) no current is induced on K or A due to the shielding effect of the grids. A current flows through the anode during the time t_3 when the electrons move towards A after crossing GA. The extension of each time interval depends on the actual strength of the electric field in the corresponding gap. A charge amplifier allows to measure the charge Q_K and Q_A from integration of the anode and cathode signals in t_1 and t_2, respectively.

7.2 UV laser calibration

Another method to perform calibration of the liquid Argon detector, and in particular the monitoring of the purity, is based on the development of a novel online method employing UV laser beams for the multi-photonic ionization of the liquid. The principle of laser calibration relies on the possibility of producing inside the LAr volume tracks that are similar to those created by ionizing particles and of which one knows (a priori) the ionization yield, the position and the time. These 'tracks' are not affected by multiple Coulomb scattering and Landau fluctuations.

Laser beams have been already widely used to measure the drift velocity in drift chambers or the space charge induced by distortions in the drift, namely under high luminosity conditions. In our application, we intend to measure the life-time of the primary ionization in the cryogenic liquid, namely the purity level reached under operation of the purification system.

A multi-photon process is one which occurs through the simultaneous absorption of two or more photons via virtual states in a medium. These processes require high peak powers which are easily available from pulsed lasers. Bound electrons may absorb several laser photons simultaneously to excite the atom to high energy levels or even to overcome their ionization potential. The number of photons required to photo-ionize an atom or a molecule is given by the ratio between the ionization potential and the photon energy, rounded up to the next integer. For instance, the ionization potential for an Argon atom is 15.76 eV whereas the photon energy at 266 nm is 4.66 eV, thus leading to a minimum number of 4 photons in order to produce ionization.

The absorption of multiple photons makes this process highly non-linear (fourth-order for Ar); its cross-section strongly reduces with the order of the process, thus making its effectiveness largely depending on the laser operating frequency. In order to produce a significant ionization in a target medium (typically gaseous), for high-order processes it is necessary to have very high intensities, which are typically achieved by focusing the laser beam. Interaction of laser with matter in the liquid phase has been comparatively less studied with respect to gas and solid phase. In particular, no measured energy level diagrams are available for elements in liquid phase whereas ab initio calculation are made difficult by the lack of an order. Nevertheless, some important features are well understood and reported in [32].

A proposal to employ UV laser calibration has been made for the ICARUS detector and a R&D programme being conducted. If successful we plan to use this calibration method for the LAr TPC detector in T2K by sending the laser beam through some of the dewar top flanges, suitably equipped with quartz windows, transparent to the laser UV light.

7.3 Slow control

8 Inner detector

8.1 Mechanical structure

The inner detector is composed of a rigid mechanical frame made of stainless-steel that is based on the cryostat floor by means of xx adjustable feet (Fig. 25). The structure is made independent from possible deformations of the cryostat occurring during the initial cooling and it is also self-supporting. The stainless-steel frame has dimensions of xx m in length, xx m in width and xxx m in height, and weights of about xx ton.

Two lateral wire-frames with the task of supporting the two (left and rigth) TPCs are positioned on the vertical long sides of the mechanical structure. The structure is designed in order to sustain without appreciable deformations the total force applied by the TPC wires.

Materials of the mechanical structure were chosen and treated to guarantee the LAr purity and the minimum radioactive The beams and the pillars of the structure are built with AISI 304L stainless-steel, while non metallic components are made of PEEK, a plastic material with excellent thermomechanical properties. Metal surfaces are passivated and all mechanical components are washed in ultrasound bath prior to installation inside the dewar.

.....

8.2 TPC read-out planes

In the baseline detector design one has two TPCs (Left and Right chamber) placed inside the cryostat along the beam direction. Each TPC consists of a system of two parallel wire planes 3 mm apart from each other. We are also considering to introduce a third wire plane in each

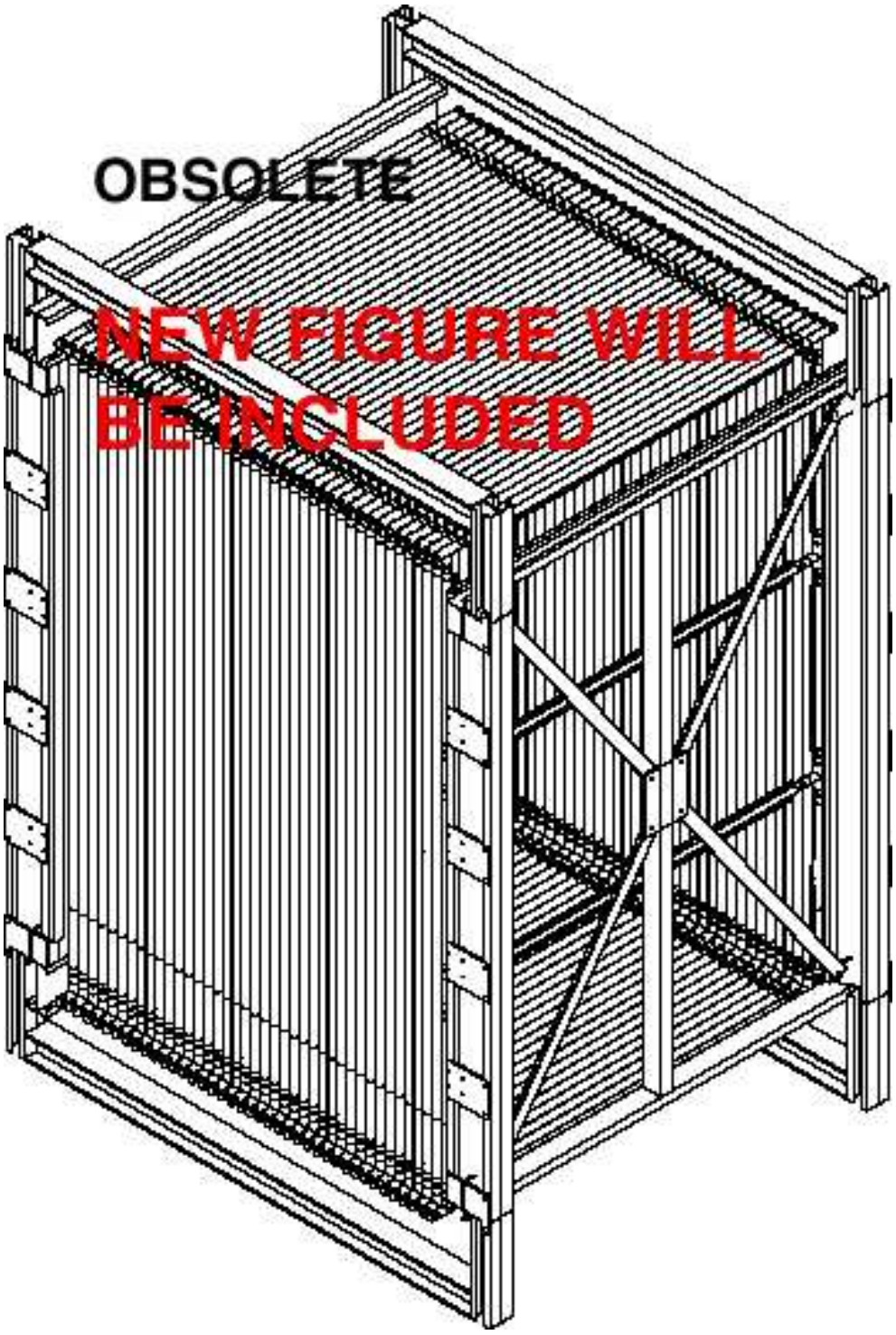

Figure 25: Layout of the inner detector supporting structure.

Number of readout chambers	2
Number of wires planes per chamber	2 (all readout)
Number of optional wires planes per chamber	1 vertical
Wires orientation respect to horizontal	$\pm 45^0$
Wires orientation respect to horizontal	90^0 (optional)
Wires pitch (normal to the wires direction)	3 mm
Wires length:	
wires @ $\pm\, 45^0$	6.6 m
wires at the borders ($\pm 60^0$)	0 m $\div$ 6.6 m
optional vertical wires (90^0)	4.67 m
Wires diameter	150 μm
Wires nominal tension	10–20 N
Number of wires / plane:	
Wires @ $\pm\, 45^0$	80
Wires at the borders ($\pm 45^0$)	2200
Optional vertical wires (90^0)	1666
Number of wires / chamber:	
@ $\pm\, 45^0$	160
at the borders ($\pm 45^0$)	4400
Optional vertical wires (90^0)	1666
Total	4560 (6226)
Total number of wires	9120 (12452)
Maximum drift length	2.33 m
Maximum drift time @1000 V / cm	1.17 ms
Distance between race tracks	50 mm
Imaging volume :	110 m^3
length	5 m
width	4.67 m
height	4.67 m
Total imaging LAr mass	**150 ton**

Table 9: Main parameters of the internal detector mechanics. In the baseline option, two planes will be instrumented. Optionally a third vertical plane could be considered.

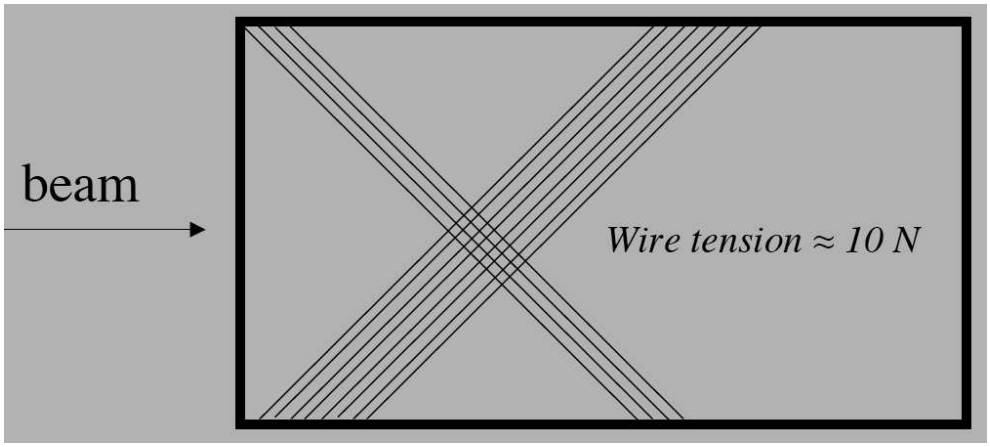

Figure 26: TPC wire planes. **FIGURE NEEDS TO BE REDONE**

chamber, in order to increase redundancy in the event reconstruction and to help in solving possible ambiguities. The increase in mechanical complexity and in the number of electronics chamber is considered to be affordable.

The distance between the two TPCs is about xx m, with the cathode plane, parallel to the wire planes, placed in the middle. This sets at xx m the maximum drift length of the active volume for both chambers.

Wire directions in the planes run at $\pm 45^o$ with respect to the horizontal direction. The planes closer (farther) to the cathode are called Induction-1 (Induction-2) planes. The wire pitch can be 2 or 3 mm according to the the different detector options.....

Wires are made of AISI 304V stainless steel with a diameter of 150 μm. They are stretched in the frame supported by the mechanical structure previously described. A set of xxxx adjacent wires all xxx m long form each of the two wire planes. The single wire capacitance is expected has to be xx pF/m. The tension applied to each wire corresponds to about xx g. Table xx lists the main features of the wire chamber system. Fig. 26 shows a view of one of the TPC chambers equipped with two wire planes.

Wires are anchored by holders onto the wire frame in groups of xxx. Holders are made of PEEK and stainless-steel. A printed circuit establishes the electric connection between wires and connector pins, in turn connected to signal cables connected to the cryostat feedthroughs.....

8.3 Wiring procedure

Text from Zalewska

8.4 Electrodes

8.5 Light read-out system

8.5.1 Scintillation light

More text from Columbia

We already mentioned that charged particles interacting in the LAr volume create ionized and excited Argon molecular states which produce scintillation radiation through recombination and de-excitation processes with with $\lambda = 128$ nm and with a yield of the order of 10^4/MeV.

missing picture

Figure 27: Scheme of the PMT supporting structure.

This prompt light signal is suitable to provide an absolute time measurement and a trigger for ionizing events occurring in LAr.

In order to detect the scintillation radiation one can employ a system of photomultiplier tubes (PMTs) directly immersed in the liquid, as already implemented for the ICARUS experiment [22].....

However, one should note that ususal PMT glass windows are not transparent to the 128 nm scintillation light. The PMTs can then be made sensitive to VUV photons by coating the windows with a proper fluorescent wavelength shifter, namely a compound which is sensitive to the 128 nm radiation with an emission probability peaked in the blue region, where the transmittance of the glass window and the photo-cathode quantum efficiency are sufficiently high. In ICARUS TetraPhenyl-Butadiene (TPB) was used [22].....

In the proposed detector for T2K we intend to mount the PMTs behind the TPC frames by means of plastic slabs and stainless steel bars as shown in Fig. 27 The number of PMTs and their actual location has been defined by simulations that took into account the tube dimensions, position and detection efficiency to VUV photons and the light transmission of the window (at 128 nm).....

A voltage divider designed to operate at low temperature can be welded directly to the PMT output leads. The PMT bases can be connected to HV feedthrough flanged on the detector signal chimneys.....

8.5.2 Cerenkov light

Might get rid of this section

8.6 High voltage systems

8.6.1 Drift voltage supply

In the LAr Time Projection Chamber each wire reads the signals from a large volume, defined by its length times the wire spacing times the total drift length. A minimal number of read out wires is achieved when choosing the maximum drift space, in this case about 4 m. At a nominal drift field of 1 kV/cm this requires a supply voltage of order 400 kV.

A simple estimate shows that the capacitance of a single cathode mounted 10 cm from the grounded walls of a detector is of order 500 pF. At 400 kV the stored energy would be 40 Joules, sufficient to vaporize parts of the structure in case of complete discharge of the cathodic plane taking place in a short time($\sim \mu sec$). Additionally, the surrounding liquid argon would instantly boil, causing a shock wave. In any case this discharge modality is quite disfavored. due to the very high dielectric rigidity of liquid argon($\sim 2\ MeV/cm$) Although not impossible, the technical challenges and the risks involved by using these high voltages are significant, especially since the

stored energy increases with the square of the voltage. As back-up solution one has to consider splitting the detector into two drift volumes with 200 kV each, but twice the number of anode wires.

If the cathode is centered in the detector, the separation from ground is very large. Additionally the reduction to only 200 kV will result in a stored energy of 0.5 Joule. Although this design would be much easier, even at 200 kV great care has to be taken to smoothen all surfaces and to round all edges to avoid local enhancements of the electrical field. Segmenting the HV system and coupling the parts with current limiting resistors might be needed to reduce the consequences in case of breakdowns.

The cathode HV has to be passed through two metal walls, first into the vacuum cryostat and then into the actual detector volume. Liquid argon has excellent properties as electrical insulator, unlike its gas phase. Thus, the HV must be supplied below the liquid level. The more severe problem is the passage through the vacuum of the cryostat. Any imperfection in surface smoothness can lead to corona discharges, which produce free electrons. Surrounding the conductors with commonly used electronegative gases, such as SF6 or CO2 which attach free electrons is excluded since these gases liquefy or solidify at the liquid argon temperature. Traveling free in vacuum the electrons will produce X-rays with a Bremsstrahlung spectrum of 400 keV endpoint energy. Even a small current of μA would produce sufficient X-rays not only to create a background source for the detector, but also to be a health hazard for personnel around the detector.

Also, passing the HV through the metal walls with hermetic feed-throughs is not easy since most of the common insulators do not support such cold temperatures. The remaining materials have thermal expansion coefficients vastly different from the metal of the detector walls. Considering all these issues it seems best at such high voltage levels to avoid the feed-throughs and the passage through vacuum altogether and generate the cathode HV locally, in vicinity of the cathode within the liquid argon.

Practically there are two schemes worthwhile to be studied in detail. The first is the fly-back transformer, best known from its use in car ignition systems and CRT HV generation in TV sets. The fast transients, however, might generate excessive noise, which is difficult to shield while detecting femto-Coulomb charge signals on the read out wires. This leaves the Greinacher/Cockroft-Walton generator, the method of choice in most commercial HV power supplies.

The Greinacher/Cockroft-Walton circuit which consists of a cascade of rectifying cells. Each cell is made of two capacitors and a diode that can withstand high voltage($1\ kV - 5\ kV$). The availability of such diodes is not a problem from technical point of view and they are not expensive at all.

So far, capacitors with size of few cm^3 designed for operation at 1kV have been found.

The limit of 1kV sets the maximum value for the voltage that each cell can provide, regardless of the fact that the diodes can withstand more.

In the baseline option of the set-up adopted so far for preliminary test(Fig 29), 1kV per cells correspond to 1kV/cm. If a higher potential gradient is desired two possible solution are available. The first is to have n cells per cm, where n is the number of kVs/cm desired. In this case the numbers of capacitors is $n * 2 * N_0$ where N_0 is the number of cells. With this solution, the volume needed for the circuit is quite large. The ripple on the DC output increase proportionally to n. The second possibility is to keep 1 cell per cm, which provide the nkV, and to share the nkV among several capacitors connected in series. Then the initial capacitance value can be restored by connecting capacitors in parallel.

With this set-up the number of capacitors increase proportionally to n*n, the cost grows

significantly but the ripple on the DC output does not change. with respect to the baseline option. The space occupied by the circuit is much less than in the previous case.

As it has been seen in a preliminary time test at LAr temperature, the capacitors can withstand two times more voltage than the value foreseen by data-sheet. If we take as an example a circuit providing $4kV$ per stage, in this case the capacitors needed to make such a circuit are only 4 times more than the baseline option, instead of 16 times.

With this set-up the ripple can be easily kept at level of $10^{-4} * V_{out}$.

Before to chose this circuit as reliable solution to the generation of HV, several problems have to be solved. One of this is the capability of the capacitors to withstand high voltage for long time.

The technical capability to realize a circuit where any possibility of discharge is disfavored is another item to pay attention on.

Successively the realization of a good screening to prevent the generation of noise on the wires read-out channels of the TPC is also needed.

In order to deal with the problem of the noise generated by the oscillating signal of the power supply circuit, which can not be avoided, some other solution are envisaged. One adopted already in the baseline option is of using an input signal at 50 Hz, being this very far from the bandwidth of any commercial preamplifier that can be operated for the wires read-out. A second and non exclusive feature with respect to the one just mentioned to reduce the noise is to synchronize the primary power circuit of the HV power supply with the trigger of the detector and to switch off the oscillating input-signal as long as the full drift and acquisition time last. The HV system can keep the full charge/voltage for long time(few days).

Another possible option for the implementation of the Greinacher/Cockroft-Walton is tho provide high voltage AC signal($10000 - 20000$ kV) and to make a circuit with few stage, for example 20 stage at 20000 V to get 400 kV.

With this option a second stage of amplification of the AC signal is needed inside the dewar. In fact, to inject by a feed-trough an AC signal whose amplitude is higher that few kV could be really challenging if not impossible.

Another draw-back of this solution is that we can polarize only field shaper each $10 - 20$ cm if we want to have a filed not higher than 1 kV/cm, but in this case the dis-uniformity region which extends almost for two times the distance between the field shaper would be much larger than what has been envisaged.

Eventually, the realization of a monitor of the output voltage is needed. Since the Greinacher/Cockroft-Walton version adopted is with no load this can not even be used for monitoring of the output voltage. In fact, any load would produce a ripple on the output not acceptable for a good running of the detector.

Then a "Field Mill"(Fig 28) apparatus is under investigation as possible solution to measure directly the field and to monitor also the uniformity of the field along the full volume where the field is made. Any failure of a stage of the Greinacher/Cockroft-Walton circuit can be detected as variation of the field generated by the cathode with respect to the ground and the cell failed can be detected by detecting the dis-uniformity of the field in the region very close to it.

The physical idea which the "'Field Mill" is based on is that a conductive plane at a vitual ground immersed in a filed move up its potential to the one due to the field in the equipotential surface where the plane is positioned. When conductive plate connected to the ground is faced to the plane to the virtual ground the field is screened the the floating conductive plane can deliver the charge accumulated to a preampliphyer. The full charge is poportional the potential and to the field. If the plane which is used toi screeen the field is driven by a motor it can preiodically screen and un-screen the field generatin a serie of repeted measurement of the filed.

Figure 28: Field Mill.

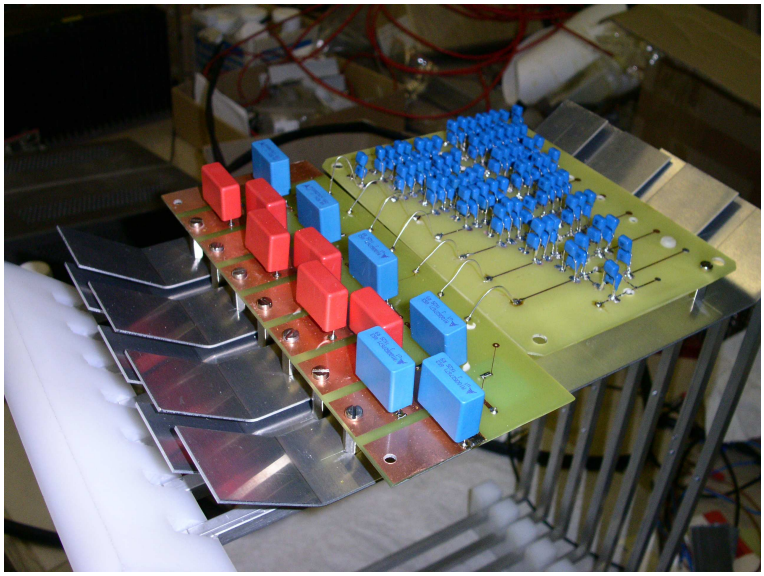

Figure 29: In the picture the power supply circuit is shown with the filter between the DC output and the race tracks.

In th Fig. 28 deteils of the "Field Mill" are visible.

In Fig 29 the picture of the first test circuit with the filtering circuit also is shown. The filter is made of the two RC in series which attenuate any ripple of he DC output of about ... dB

By using the circuit shown in the Fig 29 2 kV/cm have been reached and a test in LN_2 has been made without any problem. The capacitors($NP0$ dielectric) withstand well the cold.

Although during the design phase all solutions might be revisited, the Cockroft-Walton generator close to the cathode seems to be the best solution for safe and reliable HV supply.

8.6.2 Read-out plane biasing

8.7 Monitoring and slow control

Text from Badertscher

9 Read-out electronics

9.1 Front-end electronics

Text from Laffranchi + AR

A: Detector dewar
B: LAr Purification
C: Buffer
D: Heat exchanger and expansion valve
E: Argon pipes
F: Shock absorbers
G: Dedicated shaft (ventilation+piping)

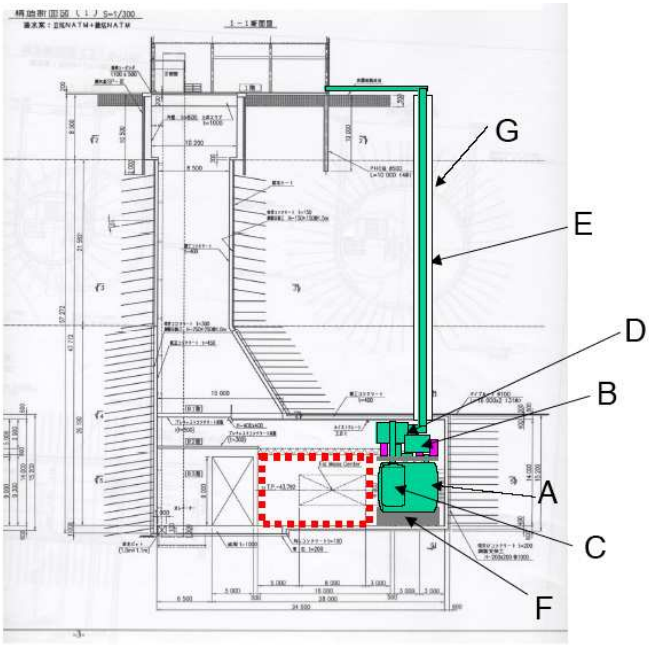

Figure 30: The infrastructure (side view).

9.2 Trigger system

9.3 DAQ system

10 Logistics and installation

10.1 The 2 km site

10.2 Site infrastructure

Item	Power requirement (upper limit)
Readout electronics	30 kW
Computers + DAQ	20 kW
Cooling	100 kW
Forced ventilation	**NOT YET DEFINED**
Uninterruptible Power Supply (UPS)	20 kW
Total	170 kW

Table 10: Estimate of electrical power requirements.

10.3 Cryogenics surface and underground equipments

B is the facility for the compressors. These should be inside a building. They are VERY noisy (80db or more). Typical example is in file cryo19.jpg. I think that one would need a surface

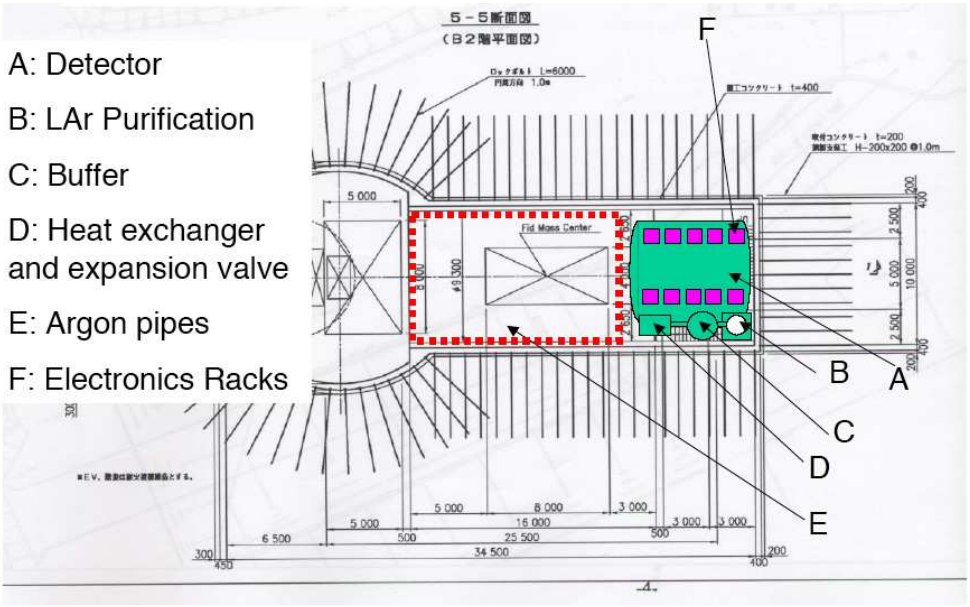

Figure 31: The infrastructure (top view).

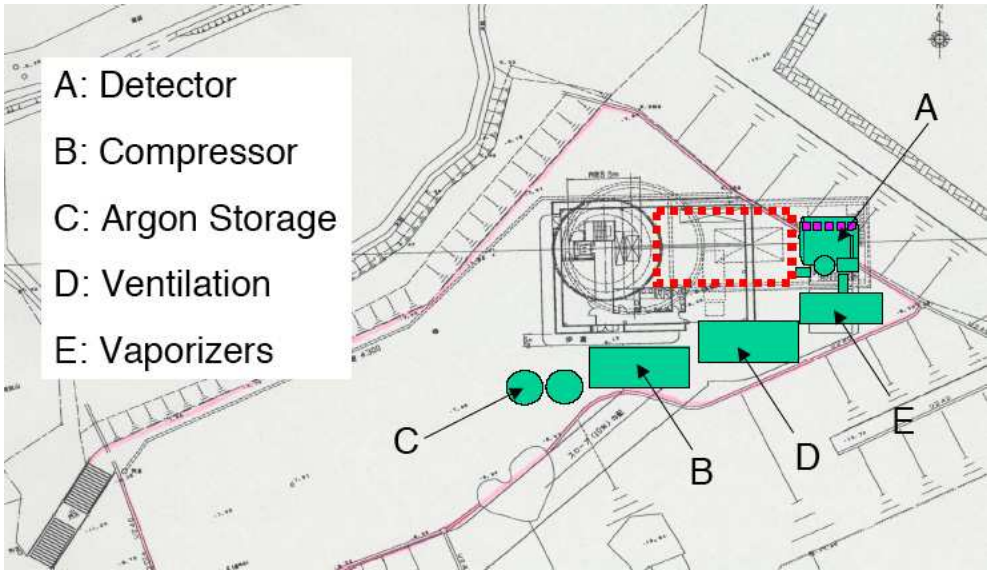

Figure 32: The infrastructure (surface equipment).

barrack of 10x10x3 m3 if possible, although it might fit in smaller space. No need for heating, on the contrary these devices will need water cooling. This is where most of the cryogenic power will be released (we said up to 100kW conservative). Note that we are still trying to design the tanker with minimal heat losses, so we still have to see what is cheapest: (a) use compressors or (b) replace the boiling-off argon with new argon. My estimate is that for more two years of operation it is cheaper to cool with compressors than to buy argon for the boil-off. On the other hand, there might be a possibility to get a very special contract with a firm in Japan close to Tokai that might be interested in selling cheap argon for ¿5 years. For such a period of time, one could get interesting offers. I always assume that argon costs about 1-3 CHF/liter (or 1-2 dollars/liter). Maybe it is less than (but no so much) that for long term contracts.

C is liquid argon storage. Typically two tankers of 5000-10000 liters each. Should be located outside.

D is the equipment needed for the forced ventilation. We still do not have a detailed scheme for that.

E are vaporizers which are heat exchangers which should be located outside. I put this because normally there is a law that says that every exhaust should be done through a vaporizer to make sure the exhaust is at room temperature before it is released in the air. For this we do not need a building.

#	Description	Characteristics
2	Storage dewar for LAr	5000 lt / unit
2	Ar compressor units	"cold" power = 3 kW / unit
1	Electrical supply cabinet	Max power = 100 kW
1	Automatic fieldbus control system racks	Automated Profibus

Table 11: Auxiliary plants installed on surface.

10.4 Safety issues and controls

Safety issues when handling liquid Argon are well known and are handled according to international standards.

The liquid Argon (or "refrigerated argon") hazards are the following: (a) contact may cause cold burns; (b) High concentration may cause asphyxiation (victims may not be aware because odorless).

It is important to take some precautionary fire measures: indeed, external fire may cause containers to rupture/explode. Argon itself is however non-flammable and all known extinguishants may be used. It is therefore important to ensure a minimum distance between the liquid Argon cryostat and other potentially flammable devices.

Another concern is the accidental release of gaseous argon in large quantities due to liquid argon evaporation: in this case, safety measures require to evacuate area and ensure adequate air ventilation. Personnel should not enter area unless atmosphere proved to be safe. If possible, one should immediately stop flow of the product. Argon gas, being heavier than air, will not evacuate from underground hall without forced ventilation. A strong forced ventilation system will therefore be installed and a dedicated vertical shaft is planned.

It is important to identify and understand the specific safety issues related to the different phases of operation.

1. Initial cooling: this is a transitory phase which will last roughly a week in which the

detector frame will be cooled down. The mass inner-detector and dewar are about 20 tons of steel. These will be cooled with argon. The amount of argon needed for cooling is about 10 LAr m^3. Hence, we expect a GAr venting of about 8350 m^3 which is about 1.7 times the size of the underground hall. Surface venting will be provided via piping and additionally the hall ventilation will be operated during this phase.

2. Thermal insulation: A closed circuit of liquid argon with compressors on surface will be controlled by the temperature/pressure of inner vessel. The heat losses under normal conditions yield a consumption of about 100 LAr lt/day. This corresponds to a power of approx. 300 W (cold) or 6kW electric. Including liquid argon purification this number increases to 500 LAr liters/day (estimated) or approximately 30kW electric. In the case of an accidental loss of vacuum insulation, the consumption should raise to 2000 LAr liters/day or about 1 m^3GAr/minute. In this case, gas will be evacuated to the surface through venting via dedicated piping and the hall ventilation.

3. Transfer lines, piping or external components failure: safety will be ensured by redundant pumps, valves, etc. Thermal stress of transfer lines resulting potentially in loss vacuum insulation of pipes will be taken into account.

4. Catastrophic failure of cryostat (unlikely): a possible cause is the event of (a) fire in the hall (b) external impact (c) Earthquake. Shock absorber will damp the effect of earthquakes. In case of rupture, one expects a "flash" production of gaseous argon due to the equilibration of the pressures. If the detector is operated at an overpressure less than 0.2 bar (this will be controlled by the external refrigerator), less than 600 m^3 will be produced, to be compared to the size of the hall of 4830 m^3. Forced ventilation will deal with the flash. Unfortunately a catastrophic failure could cause major spill of liquid Argon. By design, the liquid argon is within a double containment since both inner and outer vessel must break for argon to spill in the hall. However, this would represent a major hazard! A containment pool could provide a triple containment for maximal safety.

10.5 Electronics racks and counting rooms

10.6 Installation procedure

11 Detector operation

11.1 Detector commissioning

11.2 Running

11.3 Calibration operations

11.4 Online monitoring

12 Detector performance

12.1 Hit, cluster and track reconstruction

Charged particles traversing the LAr sensitive volume produce ionization electrons in a number proportional to the energy transferred from the particle to the LAr. The ionization electrons drift perpendicularly to the anode pushed by the electric field, inducing a current on the nearby

wires. Therefore, each wire of the readout plane records the information of the energy deposited in a segment of the ionization track.

The event reconstruction goal is to extract the physical information contained in the wires output signal, i.e. the energy deposited by the different particles and the point where such a deposition has occurred. This allows to build a complete three dimensional spatial and calorimetric picture of the event.

The basic energy deposition unit is the hit, defined as the segment of track whose energy is read by a given wire of the readout planes. Therefore, the spatial and calorimetric information of the track segment is contained in the associated hit, and the sensitivity of the detector depends entirely on the hit spatial and calorimetric resolutions.

In what follows we describe the different steps that allow us to go from single hit identification up to three dimensional track reconstruction:

Hit identification: the hits are independently searched for in every wire (disregarding, at this stage, the information provided by adjacent wires). Hits are identified as signal regions of a certain width with output values above the local mean. Every time a signal is above the local mean by more than a threshold number of ADC counts, a hit candidate is triggered. All the subsequent output samples above the threshold are added to the hit and the information about its width, i.e. the distance (in drift samples) between the hit initial and final points, stored. Rejection of fake (noise) candidates is achieved by imposing a minimal hit width value. Further noise rejection is obtained by imposing a requirement on the minimum distance between the peak position and the hit end. At the end of this stage, reconstructed hits contain the following information: view and wire indexes, width, the peak drift coordinate and height (taken as the difference, in ADC counts, between the peak and the local mean).

Fine hit reconstruction: The parameters defining the hit (position, height, area) contain the relevant physical information of the original track segment. Therefore a refined algorithm is needed to estimate these parameters in an optimal way. The adopted solution is to extract the parameter information by means of a fit that uses the following analytical function of the drift time t:

$$f(t) = B + A\,\frac{e^{\frac{-(t-t_0)}{\tau_1}}}{1+e^{\frac{-(t-t_0)}{\tau_2}}} \tag{3}$$

where B is the baseline, A the amplitude, t0 the point for which the height of the function with respect to the baseline is equal to A/2, and tau_1 and tau_2 are related to the falling and rising characteristic times, respectively. This function reproduces well the hit shape as can be seen in figure 33. This approach provides a good determination of both the hit peak (and therefore the basic information to perform the spatial reconstruction of the event) and the hit area (which is proportional to the deposited energy, so that a calorimetric measurement of the event energy can be carried out).

Cluster reconstruction: A cluster is defined as a group of adjacent hits within the wire/drift coordinate plane. The goal of the cluster reconstruction is to perform a first grouping of hits belonging to common charge deposition distributions, such as tracks or showers. Clusters provide identification criteria for the different patterns, and thus determine which reconstruction procedure must be followed. Clusters also provide a criterion, based on the cluster hit multiplicity, to discriminate among signal and noise hits,

Clusters are defined as groups of hits with links among them. A link is pair of hits coming from consecutive wires and having overlapping drift coordinate ranges, where the drift

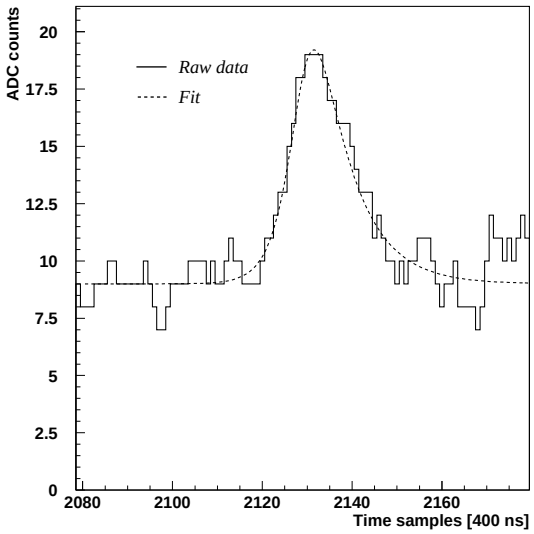

Figure 33: Example of hit fitting using equation 3.

coordinate range of a hit is defined as the one computed by the hit finding algorithm. Clusters are built in a two step approach. In the first step (pass I), preliminary clusters are built as groups of hits being connected by links. The reconstruction algorithm takes as input a list of hits from a given wire plane, and constructs all possible clusters out of them, using only the information provided by the hit finding algorithm. The second step (pass II), attempts to expand and merge the clusters found in pass I, in order to reduce the number of the resulting clusters. Attempts for cluster merging/expansion are performed along both wire and drift time coordinate directions. The algorithm proceeds as follows: first of all we check the wire coordinate. The regions around the cluster borders are examined (where a cluster border is defined as a hit linked at most with one hit within the cluster). The found cluster fragments are merged, hence reducing the fragmentation produced in pass I. When no clusters are found, new hits are searched for in the region close to the cluster borders and are added to the cluster. This reduces the cluster fragmentation caused by hit misidentification. Once no further expansion along the wire coordinate is possible for any of the existing clusters, the merging of clusters along the drift coordinate direction is attempted. Hits at the maximal and minimal drift coordinate values are compared among different clusters. Cluster merging is carried out for those pairs of clusters for which their respective minimal and maximal drift coordinate hits are in the same or consecutive wires and whose drift coordinate ranges overlap.

Three-dimensional (3D) hit reconstruction: The goal of 3D hit reconstruction is the determination of the space coordinates of the ionizing tracks traversing the LAr sensitive volume. Each wire plane constrains two spatial degrees of freedom of the hits, one common to all the wire planes (the drift coordinate) and one specific for each plane (the wire coordinate). The redundancy on the drift coordinate is the key for 3D reconstruction, since it allows the association of hits from the two wire planes to a common energy deposition. The devised 3D hit reconstruction algorithm performs efficiently on events of low track multiplicity (this will be the case for most of the events recorded with the

T2K beam). Since the outlined method is purely based on topological criteria, it is not meant to be carried out on events with more complex energy deposition patterns, such as electromagnetic or hadronic showers. For this kind of events, a method combining hit spatial and calorimetric information is being developed.

12.2 Event reconstruction, selection and classification

12.3 Particle identification

We discuss the capability a LAr TPC has to separate muons, pions, kaons and protons that decay or stop inside the active detector volume.

In order to have an efficient identification, the information provided by the particle *before* and *after* it loses all its energy and decays/stops can be combined:

- On one hand, the study of the hits recorded before (and close) to the mother particle decay/stopping vertex is essential. Because of the mass difference and for energies below the minimum ionizing value, each particle exhibits a distinct $< dE/dx >$ curve as a function of the kinetic energy which is, in most cases, sufficiently pronounced to separate them.

- On the other hand, the study of the activity after the mother particle decay vertex can be very helpful to disentangle harder (kaons) from softer (pions and muons) decaying particles. In the case of protons, the absence of decaying particles gives an even more clear signature.

The tracks were fully simulated with initial momenta of 0.5 and 1 GeV. This number is, however, not relevant since most of the distinct $< dE/dx >$ behaviour between the different kind of particles is contained in the last few centimeters before the particle decay point and in the energy deposited after this vertex. In practice this means that once the decay vertex is identified, all hits further than typically ~ 50 cm (if any) are ignored. For muons (protons) this translates on excluding momenta higher than ~ 150 MeV (~ 300 MeV).

The analysis proceeds as follows. First of all the track is reconstructed in space and split into segments. The kinetic energy of the track (T) is known from calorimetry. A good 3D reconstruction is mandatory in order to identify the different track vertexes (inelastic interactions, δ-ray emissions, decay vertex), efficiently isolate the mother particle and compute the pitch and energy ($< dE/dx >$) associated to each track segment. Then, the "$< dE/dx >$ vs. T" distribution is built and the analytical χ^2 values (difference between the experimental measurements and the Bethe-Block theoretical predictions to each particle hypothesis) evaluated. This is done using the closest segments to each hypothesis only and discarding the rest. In a further step, the particle mass is estimated by fitting the "$< dE/dx >$ vs. T" to the Bethe-Block formula (with the mass as free parameter). The χ^2 of the fit gives a direct indication of the compatibility between the measured data and the tested hypothesis. Finally, the energy measured beyond the particle decay is computed.

The designed method evaluates which one of the four tested particle hypothesis accommodates better to each individual track. The final decision is performed with the help of a Neural Network (NN) based program which is feed with the variables explained above: the analytical χ^2, the fitted mass and energy released after the particle decay.

The NN results are shown in figure 34. Plots are made in logarithmic scale in order to enhance the tails of the distributions. After the learning process, the net succeeds to identify each type of particle by assigning a high (signal-like) or small (background-like) nn_i value. At

the end, for each single event the neural net gives four numbers, the states of the four output layer neurons, and the decision of which particle type we assign to a particular event is dictated by these values. A track will be of type j if nn_j is the maximum of all nn_i, with $i = 1, ..., 4$.

This simple criteria gives excellent results as reported in figure 35. The four plots in the figure show how muon, pion, kaon and proton events (from top to bottom, respectively) get classified as muons, pions, kaons and protons (from left to right, respectively). The numbers inside the plots give the percentage of events tagged in each category.

The conclusions of this simulation analysis based on a Neural Network statistical discrimination technique shows that a LAr TPC detector presents very good particle identification capabilities, with quoted efficiencies for protons, kaons and pions-muons above 99% and contaminations below 1%. On the other hand, the muon–pion inter-contamination is found to be at the level of $\sim$25%.

12.4 Muon momentum resolution

In this section, we discuss the stand-alone measurement of the momentum of tracks via the multiple scattering method. This method can be effectively used for example for tracks escaping the detector.

For example, prompt muons emerging from ν_μ CC interactions have momenta around 1 GeV. On average, the distance traveled by those muons in liquid Argon can be as long as 3 m. Since a *m.i.p.* particle deposits approximately 200 MeV per meter, a large fraction of those muons are partially contained. In those cases, calorimetric techniques cannot be used to measure their energy. The multiple scattering method can provide a good estimate of the momentum, even in absence of an external magnetic field. Of course, escaping muons will be also measured by the downstream water detector.

In order to best employ the information coming from the multiple scattering, an estimate of the muon momenta can be obtained by using the fitting technique known as Kalman Filter (detailed discussions of the method can be found in [33, 34]).

Taking into account the information provided by multiple Coulomb scattering, the Kalman filter technique allows to measure the muon momentum on a track-by-track basis. In order to evaluate the accuracy of the method, we have fully simulated and reconstructed 1000 muons for each of the following energies: 0.5, 1, 1.5, 2, 2.5 and 3 GeV.

To compute the momentum is enough to restrict ourselves to tracks reconstructed in two dimensions. The method requires to split the track into portions, in order to get a distribution of the angular deflection due to multiple scattering. The most important parameter in the analysis is therefore the segment length. Segments must be as short as possible in order to have a large statistical sample, but at the same time they should be long enough in order to allow multiple scattering effects to emerge over the detector noise (*e.g.* measurement errors). Therefore, a compromise must be reached depending on the length of the track recorded by the detector. To improve the performance of the method, the momentum of each muon track has been computed by using three different segment lengths. The final result is obtained as an average of the three measurements.

Figs 36 and 37 show the expected resolutions as a function of both muon momentum and track length. For tracks with length less than or equal to 1 m, we have considered segment lengths of 5, 8 and 11 cm. For recorded tracks with lengths ranging between 1 and 2 m, the

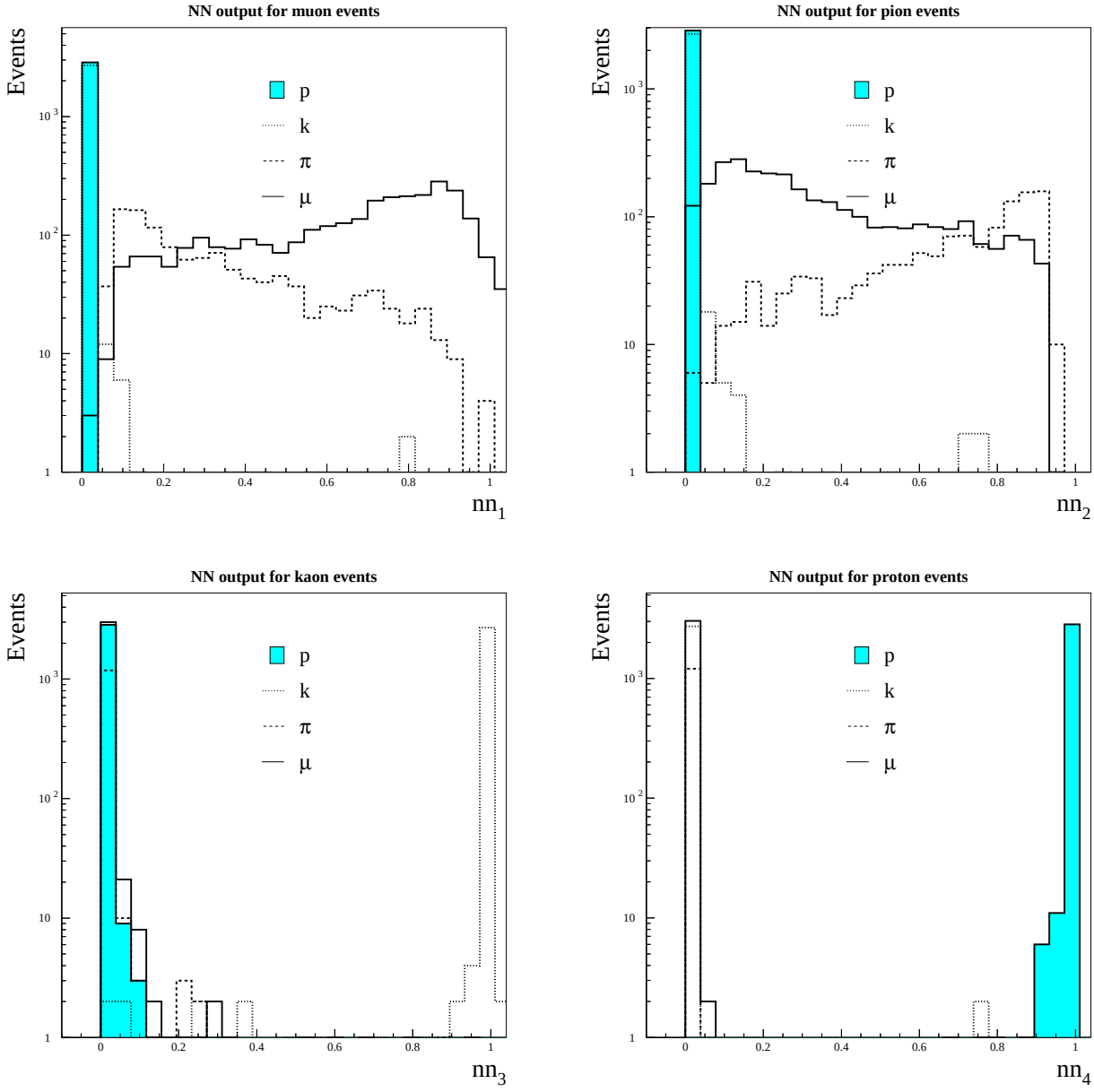

Figure 34: Multi-layer perceptron output for muons (nn_1), pions (nn_2), kaons (nn_3) and protons (nn_4). As expected, *signal* events accumulate around 1 and *background* peaks at 0.

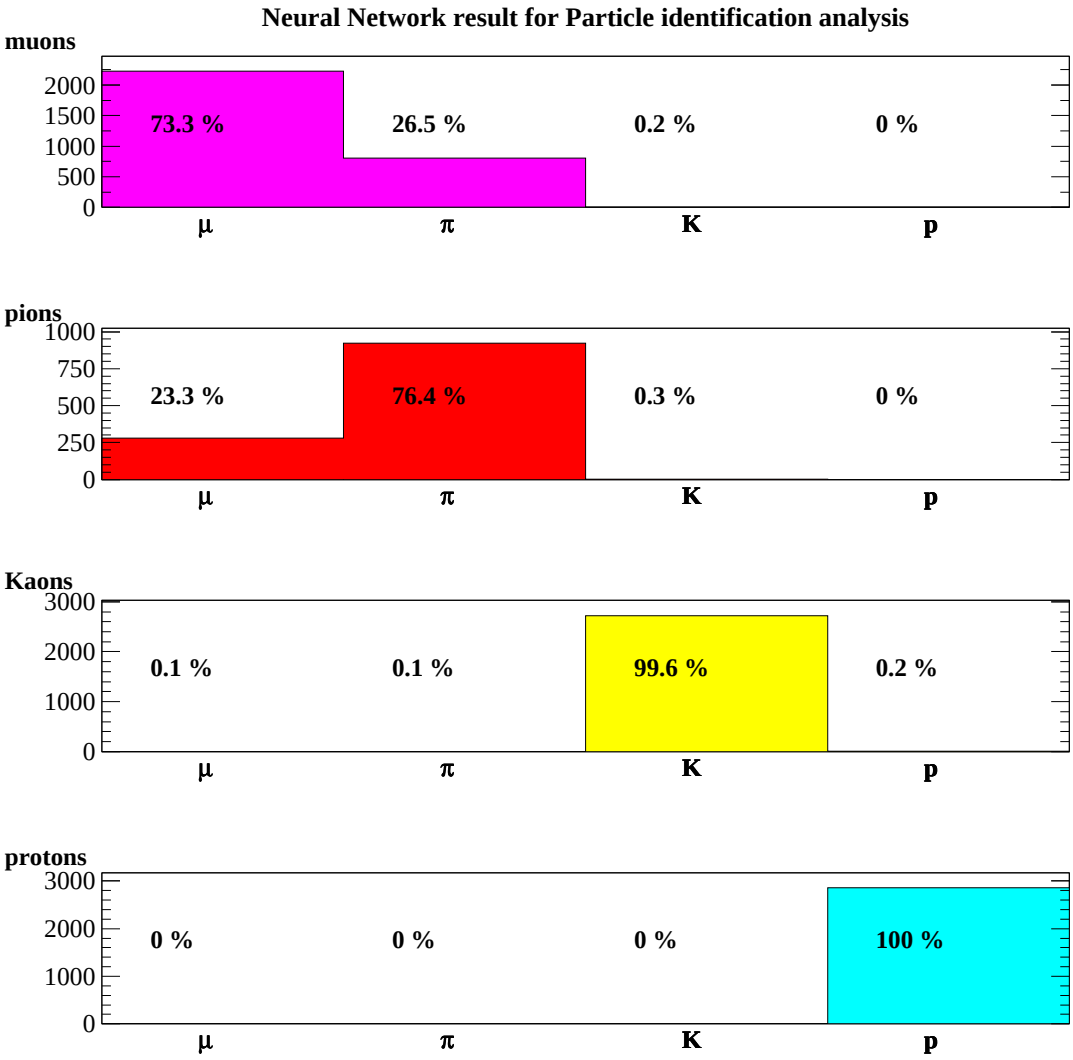

Figure 35: Multi-layer perceptron Neural Network analysis results on Particle Identification. The histograms (from top to bottom) show how each type of particle gets classified in different categories (bins from left to right).

used segment lengths are 10, 12 and 15 cm. For tracks longer than 2 m, the used lengths are 11, 15 and 18 cm.

In the left panels of Figs 36 and 37, each point corresponds to the central value obtained after fitting with a Gaussian function the distribution of measurements (1000 entries for each considered momentum). The quoted errors correspond to the RMS of the Gaussian fit. We observe that for track lengths above 1 m, all points lie within one sigma of the true generated Monte Carlo momentum. Therefore, the Kalman Filter is able to provide a reasonable estimate of the energy of partially contained particles. For shorter tracks (0.5 m in our case), a good estimation of the momentum is expected for tracks below 1.5 GeV. For larger momenta, average values fall short from the true ones.

Right panels of Figs 36 and 37 show the expected resolutions for different track lengths as a function of muon momentum. We note that for the average distance traveled by muons (*i.e.* 3 m), we expect resolutions around 15%. Resolutions are slightly improved when we consider larger distances. Note that in practice, for 0.5 GeV muons, lengths above 3 m imply that they are fully contained. This explains why, for this momentum, the expected resolution remains unchanged as track length increases. As expected, the resolution for 2 m long tracks degrades as the momentum increases, but it still remains below 20%. As we keep shortening the track, the expected resolution quickly degrades at high momentum. For 0.5 m long tracks, the resolution fluctuates between 30 and 35%.

We can conclude that for a large fraction of the neutrino events taking place in the 100 ton LAr TPC detector, the Kalman Filter technique is able to determine very accurately the momentum of individual tracks. Provided the tracks are long enough, we expect resolutions around 15%. This fact combined with the good resolution expected for the measurement of the hadronic system, means that a precise determination of the event kinematics can be obtained for events where the muon is only partially contained.

12.5 Neutrino and hadronic energy resolution

We discuss here our capability to reconstruct the neutrino energy using two different methods and compare the results.

To measure the neutrino energy it is possible to use a calorimetric approach and a tracking approach. The calorimetric approach consists simply in measuring the energy released in the detector, but this accounts only for the kinetic energy of the particles produced in the interaction; to have a precise measurement, in this range of energy, we should add the mass of the particles as well. To know the mass of the particles a traking approach is required anyway (dE/dx, neutron identification, ...). The tracking approach consist in identifying all the particles and converting the deposited energy (kinetic energy) into momentum knowing the mass. This approach relies therefore on the capability to perform a good PID.

The two methods used to reconstruct the neutrino energy studied here are based on a tracking approach and consist in:

- measuring only the muon energy.
- measuring the muon and the hadronic energy.

The former method is effective for QE events assuming a fixed kinematics (i.e. ignoring Fermi motion) and neutrino energy can be calculated as:

$$E_\nu^{rec} = \frac{m_N - \frac{m_\mu^2}{2}}{m_N - E_\mu + p_\mu cos\theta_\mu} \tag{4}$$

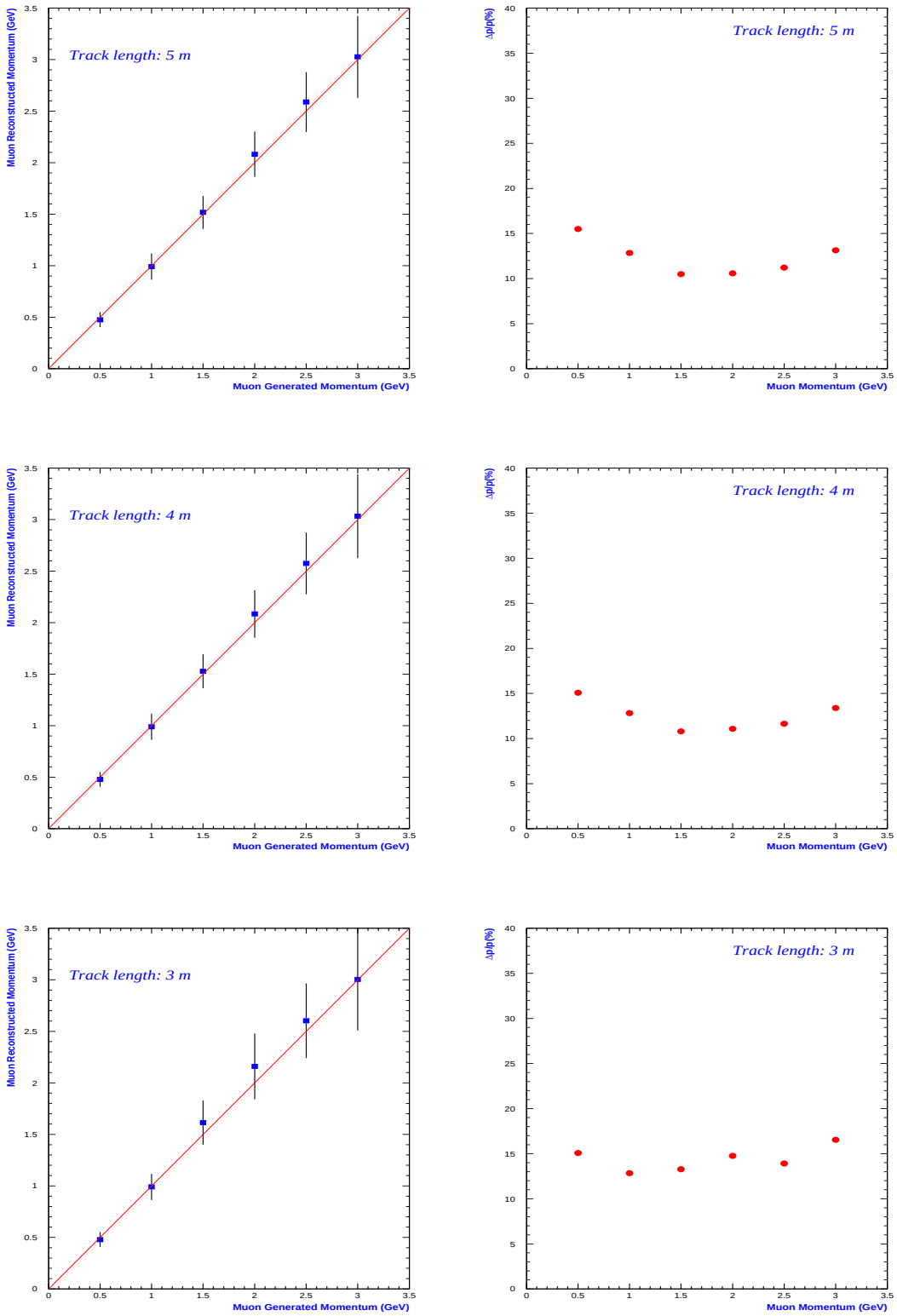

Figure 36: Left: measured momenta using the Kalman Filter versus the generated Monte Carlo momenta. Right: expected muon momentum resolution as a function of muon energy for a set of different track lengths.

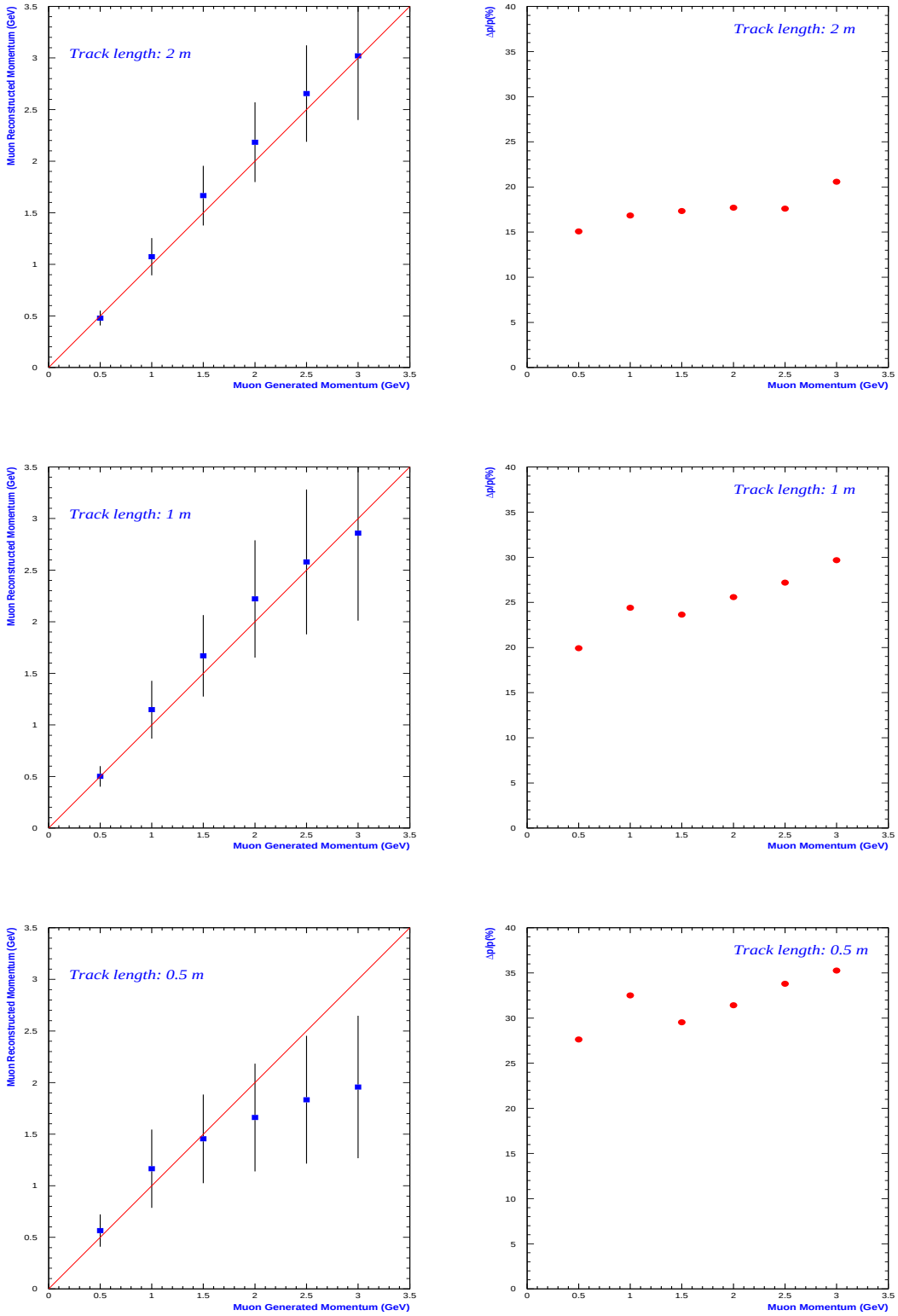

Figure 37: Left: measured momenta using the Kalman Filter versus the generated Monte Carlo momenta. Right: expected muon momentum resolution as a function of muon energy for a set of different track lengths.

The latter method relies on conservation of momentum:

$$E_\nu^{rec} = |p|_\nu^{rec} = \sqrt{(\Sigma p_x)^2 + (\Sigma p_y)^2 + (\Sigma p_z)^2} \quad (5)$$

The following assumptions have been used in our analysis:

- Since the combined use of a LAr TPC and a water Cerenkov detector allows for a very precise measurement of the muon energy, its resolution is negligible compared to the hadronic energy resolution; there is therefore no difference between hadronic energy resolution and neutrino energy resolution.
- To perform this analysis 90000 NUX generated events have been used: they contain QE and inelastic events produced in an inclusive way (i.e. using the full cross section), taking into account Fermi motion and not including reinteraction.
- All the events have been produced at the center of the detector.
- A "perfect" particle ID has been assumed, which is used to convert the deposited kinetic energy into total momentum. This PID comes from MC but relies on "matchMChits" which is a function in the reconstruction, so it has an intrinsic error.
- A perfect angular reconstruction has been assumed and we rescale the momentum components according to the ratio: $|P|_{reconstructed}/|P|_{MC}$.
- A cut-off was set on particles momentum: 310 MeV/c for protons (kinetic energy of 50 MeV) and 53.8 MeV/c for charged pions (kinetic energy of 10 MeV). At lower momenta they would produce too few hits to be identified as separate particles.

Figure 38 shows the visible neutrino energy plotted against the real energy. It is evident that, measuring only the muon, there are many events where the reconstruction is not very efficient and they are mainly non-QE events. Figure 39 shows the difference between the real neutrino energy and the reconstructed one, and the resolution on the reconstructed energy obtained using the two methods. As expected measuring the hadronic energy allows for a better resolution on the reconstructed energy. As it can be seen in the figure, there is a large number of events where the difference between the visible energy and the real one is extremely big, so we tried to eliminate it applying a cut on the visible energy of 1250 MeV, since that is the relevant range of energy for observing neutrino oscillation at T2K. The result obtained after the cut is shown in figure 40: the number of events where the reconstruction is not efficient has drastically reduced in case of full reconstruction (i.e. measuring the hadronic energy) but it is still large in case of the muon stand alone reconstruction.

The conclusion is that, measuring hadronic energy, we can reconstruct the neutrino energy with a gaussian resolution of $\sim$22%, whereas measuring just the muon energy degrade the resolution by $\sim$10% and make it non-gaussian.

12.6 Event kinematics reconstruction

One of the goal of our detector is the measurement of the QE/non-QE events ratio. To achieve it we study the kinematics of the events; in particular we analyze the distribution of the 4-momentum transferred (Q^2) and the invariant mass of the hadronic system (W), and our

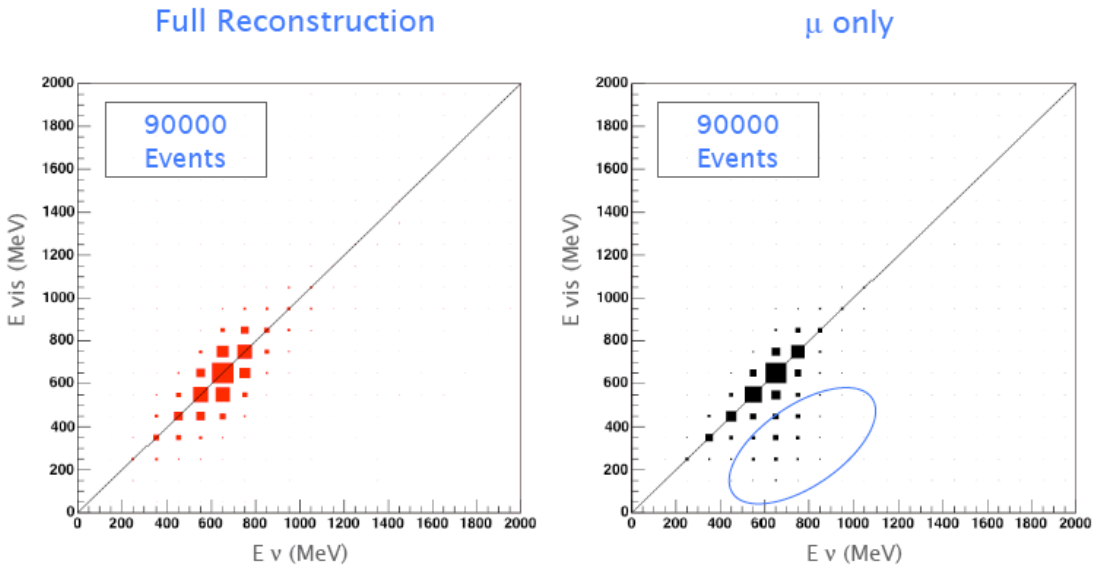

Figure 38: Visible energy Vs real neutrino energy obtained measuring both muon and hadronic energy (left) and only the muon energy (right). The region selected (right) contains mainly non-QE events not well reconstructed measuring only the muon energy.

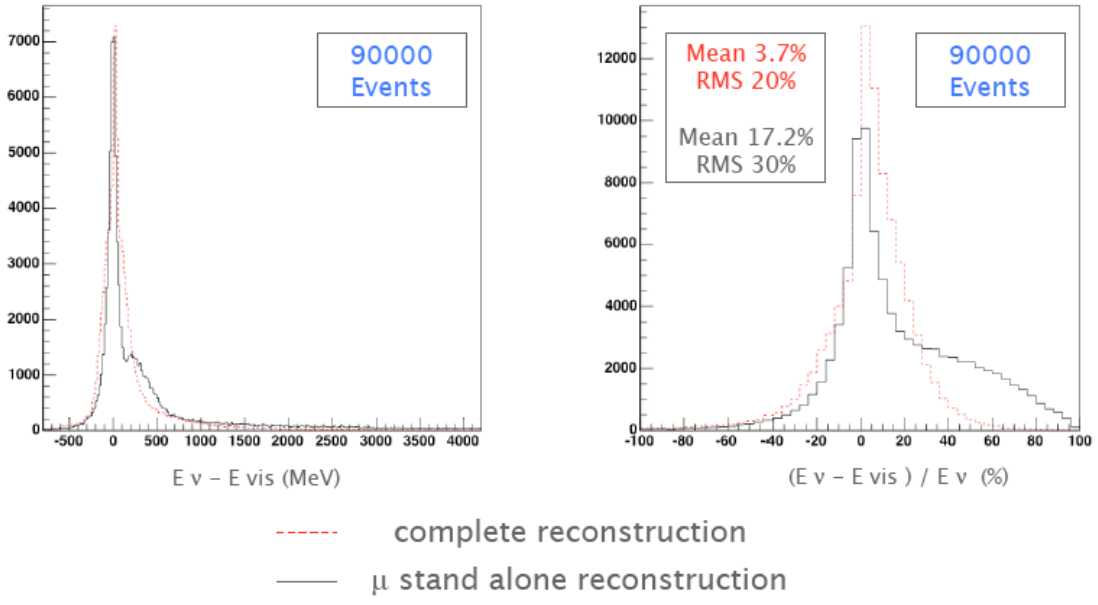

Figure 39: Difference between real neutrino energy and reconstructed energy (left), and resolution on the reconstructed energy (right). The solid gray line shows the results obtained measuring only the muon whereas the dashed red line shows the results obtained taking into account hadronic energy.

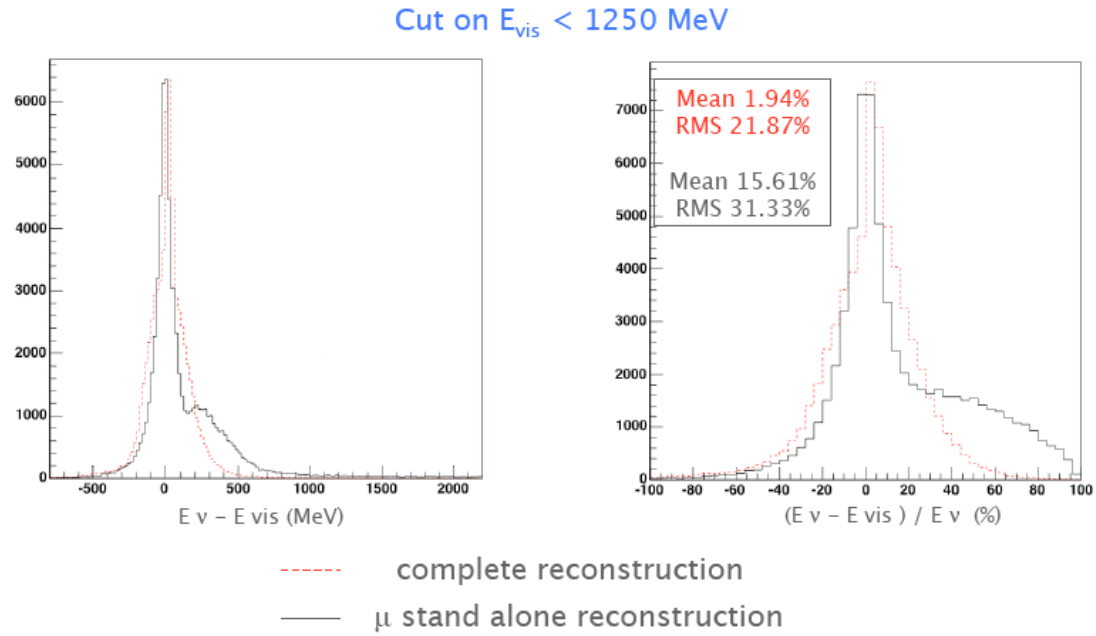

Figure 40: Difference between real neutrino energy and reconstructed energy (left), and resolution on the reconstructed energy (right) after applying a cut on visible energy of 1250 MeV. The solid gray line shows the results obtained measuring only the muon whereas the dashed red line shows the results obtained taking into account hadronic energy.

capability in reconstructing them.

$$Q^2 = E_\nu E_\mu \sin^2 \frac{\theta}{2} \tag{6}$$

$$W^2 + Q^2 = 2M\nu + M^2 \tag{7}$$

$$\nu = E_{had} - M = E_\nu - E_\mu \tag{8}$$

The analysis has been carried out using the same events and assumptions described in the previous section.

In figure 41 the invariant mass distribution obtained from MC information (generator level) is compared to the distribution obtained after applying the reconstruction process. From figure 42 it is possible to see how the reconstruction process affects the resolution on the invariant mass of the hadronic system. It is evident that in case of QE events the resolution on W in not affected at all by the reconstruction process, whereas it is slightly affected in case of non-QE events.

The same analysis has been carried out on the distribution of 4-momentum transferred. In figure 43 the distribution of Q^2 is shown with and without the effects of the reconstruction, whereas in figure 44 the resolution obtained in each case is shown. Once again, for QE events the resolution is not affected by the reconstruction process, whereas for non-QE events it is slightly degraded.

The conclusion is that given the resolution that we obtain on Q^2 (∼16%) and W (∼10%) the discrimination between QE and non-QE events seems quite promising.

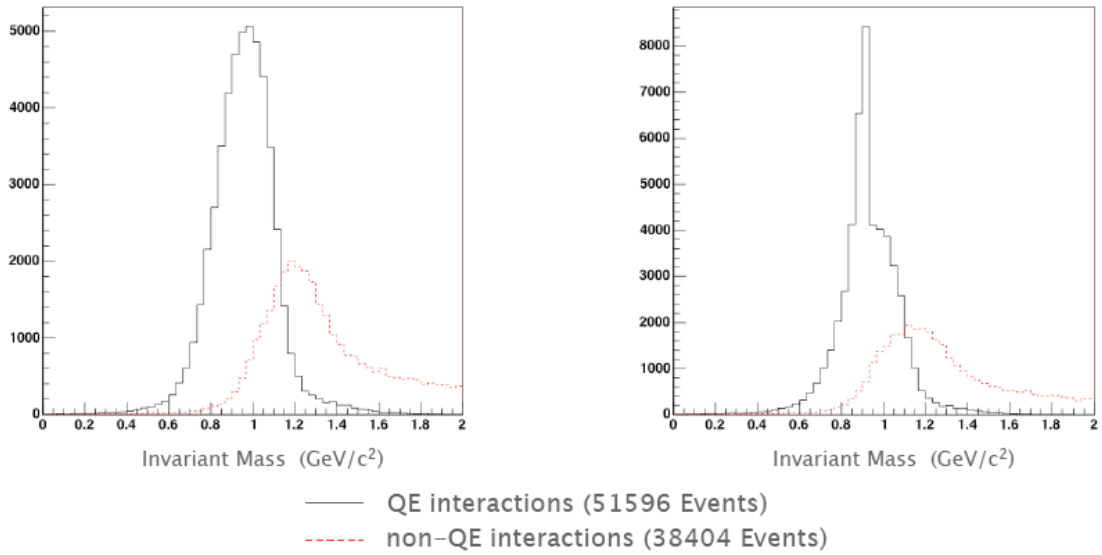

Figure 41: Invariant mass reconstructed from MC information at generator level (left) and after applying the reconstruction process (right). The solid grey line shows QE events whereas the dashed red line shows non-QE events.

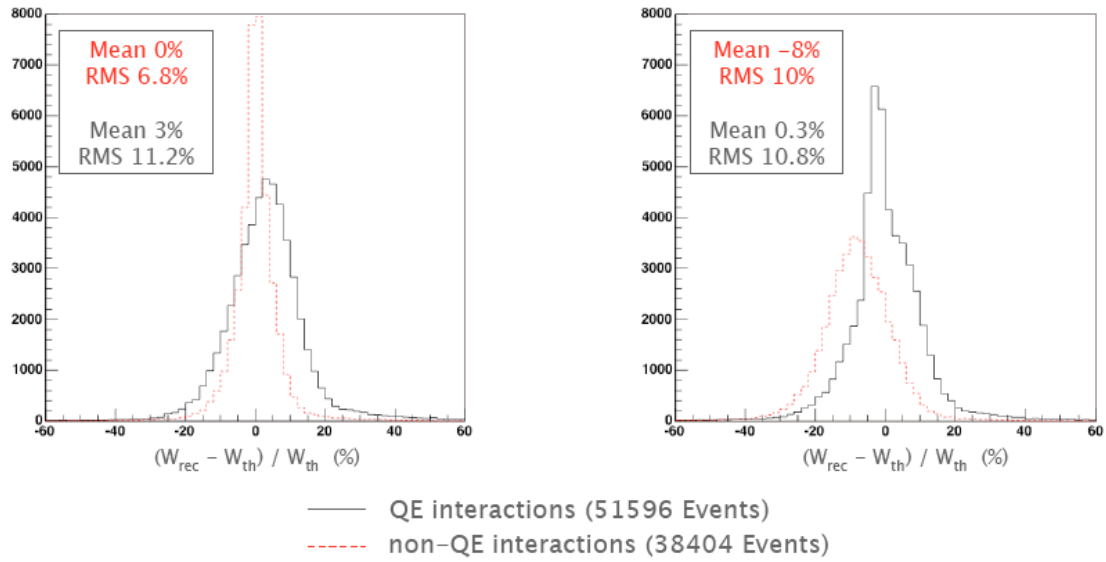

Figure 42: Resolution on the invariant mass reconstructed from MC information at generator level (left) and after applying the reconstruction process (right). The solid grey line shows QE events whereas the dashed red line shows non-QE events.

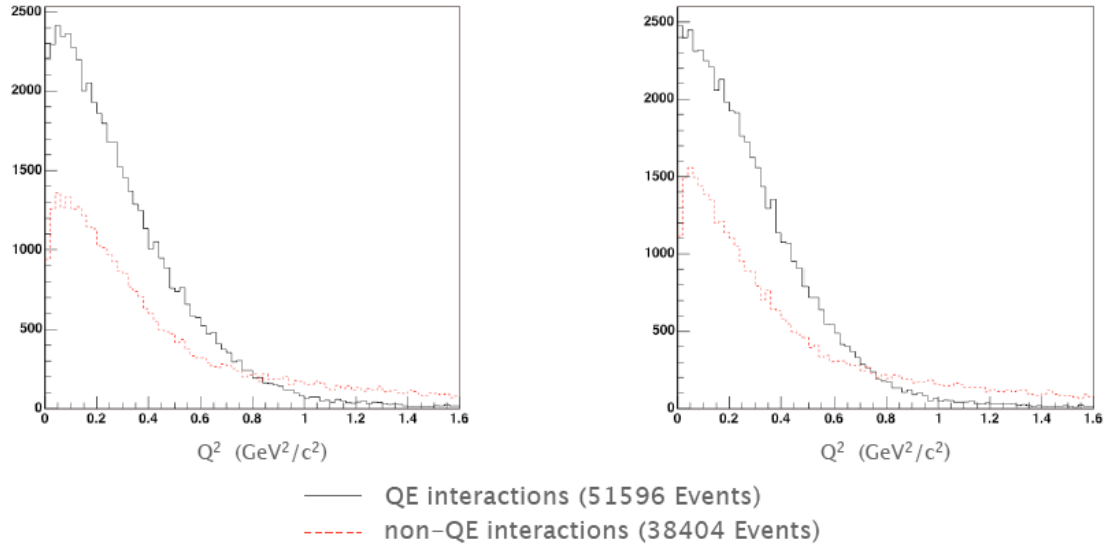

Figure 43: 4-momentum transferred reconstructed from MC information at generator level (left) and after applying the reconstruction process (right). The solid grey line shows QE events whereas the dashed red line shows non-QE events.

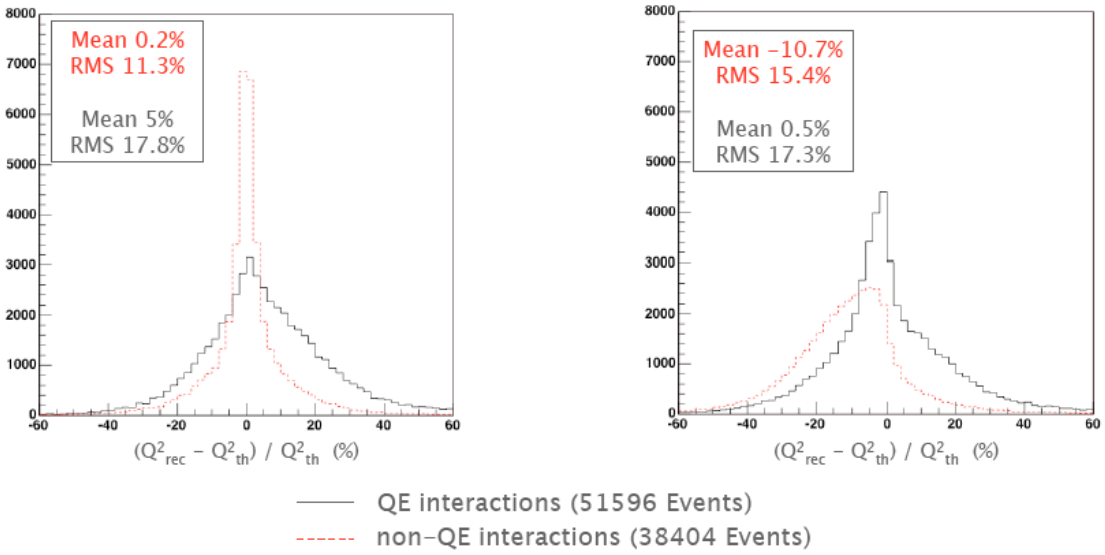

Figure 44: Resolution on the 4-momentum transferred reconstructed from MC information at generator level (left) and after applying the reconstruction process (right). The solid grey line shows QE events whereas the dashed red line shows non-QE events.

12.7 Events in the additional target

13 Physics program

13.1 Measurement of ν_μ CC events

measurement of the off-axis flux

13.2 Measurement of ν NC events

measurement of the π^0 production

13.3 Measurement of ν_e CC events

measurement of the flux

13.4 Prediction of ν_μ CC interactions at Super-Kamiokande

The predicted number of muon charged current events (at this stage we neglect backgrounds) in the 1 kt Water Cerenkov detector as a function of energy E can be formally written as

$$N_{1kt}(E) = N_A M_{1kt} \int R^{WC}\left(E, E'\right) \phi_{2km}(E') \sigma^{H2O}(E') dE' \tag{9}$$

where ϕ_{2km} is the integrated neutrino flux at 2 km, σ^{H2O} is the neutrino cross-section on Water, $R^{WC}\left(E, E'\right)$ is the response function of the Water Cerenkov detector, M_{1kt} the target mass, and N_A is the Avogadro number. The response function can be quite generally understood as the energy measurement degradation introduced by the finite resolution of the detector and by nuclear reinteraction. Note that nuclear effects also alter the cross-section (Pauli blocking, ...).

In order to perform the disappearance measurement at SuperKamiokande, the flux at Superkamiokande is predicted to be

$$N_{SK}(E) = N_A M_{SK} \int R^{WC}\left(E, E'\right) \phi_{295}(E') \sigma^{H2O}(E') P_{\nu_\mu \to \nu_\mu}(\Delta m^2, \sin^2 2\theta_{23}, E') dE' \tag{10}$$

$$= N_A M_{SK} \left(\frac{L_2}{L_{SK}}\right)^2 \int R^{WC}\left(E, E'\right) \phi(E') \sigma^{H2O}(E') P_{\nu_\mu \to \nu_\mu}(\Delta m^2, \sin^2 2\theta_{23}, E') dE' \tag{11}$$

where we stress that the oscillation probability depends on E' and where we have taken the advantage of the fact that at the 2 km position:

$$\phi_{2km}(E') = \left(\frac{L_{SK}}{L_2}\right)^2 \phi_{295km}(E') \equiv \phi(E') \tag{12}$$

A precision measurement of the oscillation parameters requires a precise knowledge of these numbers. It is clear that one must know the factor $R^{WC}\left(E, E'\right) \phi(E') \sigma^{H2O}(E')$ as a function of the true neutrino energy E'. We consider in the following the role of the liquid Argon detector in extracting this function.

We note that since the fluxes at 2 km and 295 km are essentially the same, there is no need to deconvolute separately the flux and the cross-section but rather we consider the following product:

$$\left[\phi \sigma^{H2O}\right](E') \tag{13}$$

Hence,

$$N_{SK}(E) = N_A M_{SK} \left(\frac{L_2}{L_{SK}}\right)^2 \int R^{WC}\left(E, E'\right) \left[\phi\sigma^{H2O}\right](E') P_{\nu_\mu \to \nu_\mu}(\Delta m^2, \sin^2 2\theta_{23}, E') dE' \quad (14)$$

From here, the important task is to determine (a) the response function in the Water Cerenkov $R^{WC}\left(E, E'\right)$ and (b) the product $\left[\phi\sigma^{H2O}\right](E')$.

For events occurring in Argon, the liquid Argon detector will measure the following rate as a function of energy:

$$N_{LAr}(E) = N_A M_{LAr} \int R^{LAr}\left(E, E'\right) \phi_{2km}(E') \sigma^{Ar}(E') dE' \quad (15)$$

$$= N_A M_{LAr} \int R^{LAr}\left(E, E'\right) \left[\phi\sigma^{Ar}\right](E') dE' \quad (16)$$

At this stage, we can take advantage of the high granularity of the detector to measure the hadronic energy (see Section 12.5) and the low particle detection threshold to classify events (See Section **??**). We consider for the moment two classes (QE and non-QE) which are indexed by α:

$$\begin{aligned} N_{LAr}(E) &= N_A M_{LAr} \sum_\alpha \int R^{LAr}_\alpha\left(E, E'\right) \left[\phi\sigma^{Ar}_\alpha\right](E') dE' \quad (17) \\ &= N_A M_{LAr} \left(\int R^{LAr}_{QE}\left(E, E'\right) \left[\phi\sigma^{Ar}_{QE}\right](E') dE' + \int R^{LAr}_{nQE}\left(E, E'\right) \left[\phi\sigma^{Ar}_{nQE}\right](E') dE' \right) \end{aligned}$$

where σ^{Ar}_α are the quasielastic and non-quasielastic cross-sections on Argon.

Even in the fine grain LAr, one simulate the Cerenkov thresholds of particles (i.e. essentially neglect the hadronic system) and calculate the number of events as a function of energy, *where energy is estimated using only the muon momentum*:

$$\begin{aligned} N^\mu_{LAr}(E) &= N_A M_{LAr} \int R^{LAr}_\mu\left(E, E'\right) \left[\phi\sigma^{Ar}\right](E') dE' \quad (18) \\ &= N_A M_{LAr} \int R^{WC}\left(E, E'\right) \left[\phi\sigma^{Ar}\right](E') dE' \quad (19) \end{aligned}$$

where in the second line we have used the R^{WC} response function, *since the muon is unaffected by nuclear reinteraction*, and we have assumed that the difference of muon momentum resolution between water Cerenkov and liquid Argon is negligible. Even if the hadronic system is not used in the estimation of the energy, it can still be used to classify events, hence, the liquid Argon TPC can provide the following quantity:

$$\begin{aligned} N^\mu_{LAr}(E) &= N_A M_{LAr} \sum_\alpha \int R^{WC}_\alpha\left(E, E'\right) \left[\phi\sigma^{Ar}_\alpha\right](E') dE' \quad (20) \\ &= N_A M_{LAr} \left(\int R^{WC}_{QE}\left(E, E'\right) \left[\phi\sigma^{Ar}_{QE}\right](E') dE' + \int R^{WC}_{nQE}\left(E, E'\right) \left[\phi\sigma^{Ar}_{nQE}\right](E') dE' \right) \end{aligned}$$

Finally, we can use the events occurring in the additional water target (called here WT, see Section 12.7) embedded in the liquid Argon detector. This gives:

$$N_{WT}(E) = N_A M_{WT} \left(\int R^{WT}_{QE}\left(E, E'\right) \left[\phi\sigma^{H2O}_{QE}\right](E') dE' + \int R^{WT}_{nQE}\left(E, E'\right) \left[\phi\sigma^{H2O}_{nQE}\right](E') dE' \right)$$

where we have assumed that the event classification is possible since many products of the hadronic system will emerge from the target into the imaging region (see Section 12.7). We note that the response function in the WT target and measured in the liquid Argon yields a function which (1) contains the resolution introduced by reinteraction on Water, (2) the measurement resolution of liquid Argon and (3) the calculated degradation of the energy resolution due to the passive nature of the WT. Hence, one can write:

$$R^{WT}\left(E,E'\right) = R^{LAr}\left(E,E'\right) G(E,E') N^{H2O} Ar(E,E') \tag{21}$$

where G takes into account the unobserved particle stopping in the WT and $N^{H2O}Ar(E,E')$ the difference of reinteraction between water and Argon.

One can also only consider the muon momentum to estimate the neutrino energy and get a spectrum directly comparable to that obtained in water Cerenkov detectors (!):

$$\begin{aligned} N^{\mu}_{WT}(E) &= N_A M_{WT} \int R^{WT}_{\mu}\left(E,E'\right)\left[\phi\sigma^{H2O}\right](E')dE' &(22)\\ &= N_A M_{WT} \int R^{WC}\left(E,E'\right)\left[\phi\sigma^{H2O}\right](E')dE' &(23)\end{aligned}$$

Summarizing, the event rate at SuperKamiokande is

$$N_{SK}(E) = N_A M_{SK}\left(\frac{L_2}{L_{SK}}\right)^2 \int R^{WC}\left(E,E'\right)\left[\phi\sigma^{H2O}\right](E') P_{\nu_\mu\to\nu_\mu}(\Delta m^2, \sin^2 2\theta_{23}, E')dE' \tag{24}$$

and that in the 1 kton Water Cerenkov is

$$N_{1kt}(E) = N_A M_{1kt} \int R^{WC}\left(E,E'\right)\left[\phi\sigma^{H2O}\right](E')dE' \tag{25}$$

All the terms in this convolution will be accessible via the following measurements which probe the different relevant pieces in the integral:

$$\begin{aligned} N_{LAr}(E) &= N_A M_{LAr}\left(\int R^{LAr}_{QE}\left(E,E'\right)\left[\phi\sigma^{Ar}_{QE}\right](E')dE' + \int R^{LAr}_{nQE}\left(E,E'\right)\left[\phi\sigma^{Ar}_{nQE}\right](E')dE'\right)\\
N_{WT}(E) &= N_A M_{WT}\left(\int R^{WT}_{QE}\left(E,E'\right)\left[\phi\sigma^{H2O}_{QE}\right](E')dE' + \int R^{WT}_{nQE}\left(E,E'\right)\left[\phi\sigma^{H2O}_{nQE}\right](E')dE'\right)\\
N^{\mu}_{LAr}(E) &= N_A M_{LAr}\left(\int R^{WC}_{QE}\left(E,E'\right)\left[\phi\sigma^{Ar}_{QE}\right](E')dE' + \int R^{WC}_{nQE}\left(E,E'\right)\left[\phi\sigma^{Ar}_{nQE}\right](E')dE'\right)\\
N^{\mu}_{WT}(E) &= N_A M_{WT}\left(\int R^{WC}_{QE}\left(E,E'\right)\left[\phi\sigma^{H2O}_{QE}\right](E')dE' + \int R^{WC}_{nQE}\left(E,E'\right)\left[\phi\sigma^{H2O}_{nQE}\right](E')dE'\right)\end{aligned}$$

where

$$R^{WT}\left(E,E'\right) = R^{LAr}\left(E,E'\right) G(E,E') N^{H2O} Ar(E,E') \tag{26}$$

From the above expressions, the importance of the separation between QE and nQE events is apparent. We note that this separation does not need to be on an event-by-event basis, but that statistically one can enhance or deplete the population of QE and nQE events in our event sample in order to study separately the two terms in the integrals. There are several ways to do this:

1. by an appropriate cut on kinematical variables like E_{had}, W^2, Q^2, etc.;

2. by a selection based on exclusive final state topologies;

3. naturally by the binning of events of different energies, since the ratio of QE to nQE depends on the neutrino energy.

By calling $\epsilon_{QE}(E')$ (resp. $\epsilon_{nQE}(E')$) the efficiencies to select each sample after a set of predefined cuts, we obtain:

$$\begin{aligned}
N_{LAr}(E) &= N_A M_{LAr} \left(\int \epsilon_{QE}^{LAr} R_{QE}^{LAr} \left[\phi\sigma_{QE}^{Ar}\right] dE' + \int \epsilon_{nQE}^{LAr} R_{nQE}^{LAr} \left[\phi\sigma_{nQE}^{Ar}\right] dE' \right) \\
N_{WT}(E) &= N_A M_{WT} \left(\int \epsilon_{QE}^{WT} R_{QE}^{WT} \left[\phi\sigma_{QE}^{H2O}\right] dE' + \int \epsilon_{nQE}^{WT} R_{nQE}^{WT} \left[\phi\sigma_{nQE}^{H2O}\right] dE' \right) \\
N_{LAr}^{\mu}(E) &= N_A M_{LAr} \left(\int \epsilon_{QE}^{LAr} R_{QE}^{WC} \left[\phi\sigma_{QE}^{Ar}\right] dE' + \int \epsilon_{nQE}^{LAr} R_{nQE}^{WC} \left[\phi\sigma_{nQE}^{Ar}\right] dE' \right) \\
N_{WT}^{\mu}(E) &= N_A M_{WT} \left(\int \epsilon_{QE}^{WT} R_{QE}^{WC} \left[\phi\sigma_{QE}^{H2O}\right] dE' + \int \epsilon_{nQE}^{WT} R_{nQE}^{WC} \left[\phi\sigma_{nQE}^{H2O}\right] dE' \right)
\end{aligned}$$

In the ideal case, a "quasi-elastic" selection would give $\epsilon_{QE} \approx 1$ and $\epsilon_{nQE} \approx 0$ allowing to study each sample separately.

As concluding remark, we stress that in all these arguments we have heavily profited from the fact that the neutrino flux at 2 and 295 km are expected to be the same in absence of oscillations. Otherwise the fluxes would have to be deconvoluted as well.

13.5 Prediction of electron appearance background at Super-Kamiokande

high energy muon neutrinos from kaon decays for an extra handle on the ν_e component of the beam;

13.6 Standard model neutrino interactions in the GeV region

Conventional neutrino scattering from the bubble chamber era provided the first ever neutrino data in the 1-50 GeV neutrino energy regime. This rich energy regime spans the elastic, quasi-elastic, resonance, and deep inelastic scattering regions. However, large systematics primarily from neutrino flux uncertainties, limited these measurements particularly in the interesting low-energy region. Figure 45 shows total neutrino cross section as a function of energy with contributions from different channels overlayed. Data at the lowest energies, where fluxes and cross sections are dropping off, have the largest uncertainties.

Recent neutrino oscillation experiments, with well understood, intense beams unavailable in the bubble chamber era have rekindled interest in conventional neutrino scattering physics measurements. However, recent experiments studying this energy regime lack the bubble-chamber detector precision. A Liquid Argon TPC in the T2K beam provides an excellent opportunity to study these low energy neutrino cross sections by bringing together all of the necessary ingredients for these measurements. Specifically, by combining a clean, well-understood, low energy, intense beam with a fine-grained detector, both statistical and systematic errors can be minimized.

These cross sections must be well understood not only as inputs for neutrino oscillation experiments, but also because they are interesting in their own right. The impact of these measurements on the oscillation analysis is discussed in detail in Section XXX. Following is a description of what, in addition to oscillations, neutrino scattering can teach us about the Standard Model and beyond. The T2K off axis beam peaks around 700 MeV with a very small

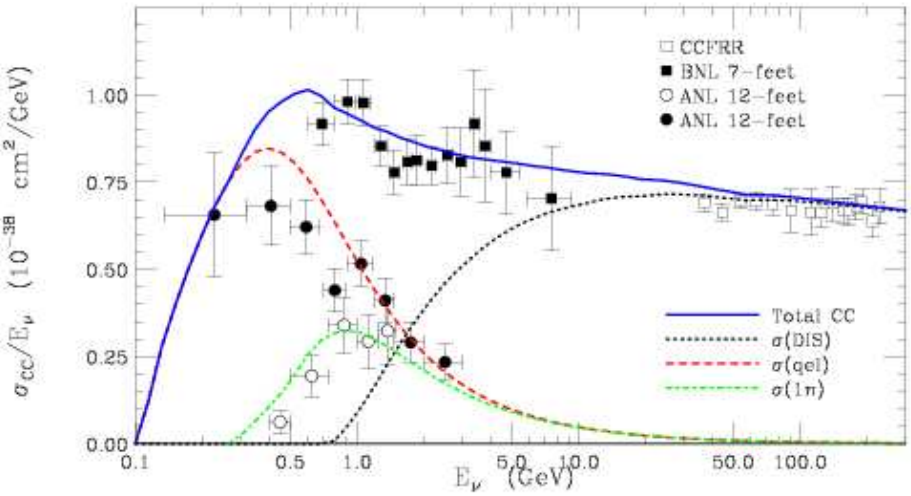

Figure 45: Cross Section/Energy versus Energy in the 0.1-100 GeV neutrino energy range [35]. Below 1 GeV, quasi-elastic scattering dominates with significant contributions from single pion production. Above 1 GeV, deep inelastic scattering turns on.

higher energy tail. This makes this beam ideal for studying the elastic and resonant channels, below deep inelastic scattering backgrounds.

- Charged current quasi-elastic (CCQE) interactions: Because of the large cross section for quasi-elastic scattering at these energies, relative to other channels, there is more data in this channel than any other from previous neutrino experiments. However, the data below 2 GeV is primarily on light targets. At T2K, these interactions will comprise about 50% of all events. Measurements of this channel in a LArTPC can improve on the existing data both with an improved resolution from the fine-grained LArTPC measurements as well as the ability to unfold nuclear effects. Recent data from K2K and MiniBooNE [36, 37] show a discrepancy at low Q^2, where nuclear effects are large, between the data and model predictions. Possible explanations for the model deficiencies include implementation of pauli suppression models and nuclear shadowing models. From precise measurement of energy and direction of BOTH final state particles, the leading muon and the recoil proton, both the neutrino energy E_ν and the Q^2 of the reaction can be determined. The shape of the differential cross-section $d\sigma/dQ^2$ is thus constrained, with a single free parameter M_A to be fitted from data. The LArTPC capability of fully identifing and reconstructing the CCQE signature, in particular, at a very low energy threshold for proton recoil detection ($T_p \leq 50-100$ MeV), is crucial to efficiently separating the CCQE signal from non CCQE interactions in order to solve the present low-Q^2 problem.

- Neutral Current π^0 Production: π^0s can be produced in neutrino interactions via resonant or coherent scattering. In coherent interactions, the neutrinos scatter of the entire nucleus rather than off of individual constituents as in the case of resonant production. Models for both coherent and resonant production are poorly constrained with so little experimental data that experiments typically assign 25-30% uncertainties on resonant production. Because predictions for coherent production rate differ by as much as a factor of 20 [38], experiments typically assign 100% uncertainty to this interaction channel. The relative

rate of coherent to resonant change as a function of Q^2 as well as for neutrino versus anti-neutrino interactions. New precision measurements with fine-grained detectors are a must to better constrain the models and understand shape dependencies. At T2K, these events comprise approximately 6% of neutrino interactions on Argon. The final data sample, for 10^{21} protons on target, will be comparable to existing samples from MiniBooNE. However, the resolving power of the LArTPC can better differentiate these interactions from background providing clean samples. Furthermore, energy resolution of these events as well as a low energy threshold can help to well measure the Q^2 dependencies for resonant versus coherent in neutrino versus anti-neutrino modes.

- Neutral Current Elastic Scattering: Neutral current elastic events comprise approximately 15% of the total event sample in the LArTPC. Through this channel, the strange axial form factor at low Q^2 can be measured and, with extrapolation to $Q^2 = 0$, the spin carried by the strange quarks in the nucleon, Δs can be determined. This measurement, crucial to understanding the spin structure of the nucleon, has suffered from model dependent measurements, for example, via polarized deep inelastic scattering [39]. Low Q^2 neutrino elastic scattering provides a theoretically robust, clean method for determining Δs. A LArTPC at T2K brings together the necessary ingredients to greatly improve upon the only previous measurement of Δs via neutral current neutrino scattering, BNL734 [40]. This previous measurement suffered from large uncertainties in the neutrino flux as well as limitations in Q^2 range. Ideally, the measurement is performed as low in Q^2 as possible to minimize the extrapolation to $Q^2 = 0$, however, uncertainties in nuclear effects limit measurements at lower Q^2 values than the 0.2GeV^2 [41] possible with this beam and detector. Specifically, the T2K beam provides a clean, low energy neutrino spectrum ideal for this measurement both in that there is a large sample of low Q^2 neutral current event and that the off axis beam has a very small low energy tail minimizing backgrounds from neutral current π^0 production and deep inelastic scattering events. The LArTPC detection technique further reduces backgrounds by possible measurement of the background $\nu n \to \nu n$ content in the $\nu p \to \nu p$ sample. Anti-neutrino running at T2K would further constrain this measurement as the form factors describing $\nu p \to \nu p$ scattering vary as a function of Q^2 for neutrino versus anti-neutrino running.

14 Integration with the other T2K detectors

15 Schedule and planning

16 Cost, funding and responsibilities

17 Conclusions

References

[1] M.H. Ahn et al., Phys. Rev. Lett. B90 (2003) 041801.

[2] http://www-sk.icrr.w-tokyo.ac.jp/doc/sk/index.html

[3] SK atmospheric oscillation signal

[4] latest k2k results

[5] http://www-numi.fnal.gov/forscientists.html

[6] M. Apollonio et al., Phys. Lett. B466, (1999) 415.

[7] http://www.cern.ch/icarus/

[8] http://operaweb.web.cern.ch/operaweb/index.shtml

[9] Y. Itow *et al.*, arXiv:hep-ex/0106019.

[10] Particle Data Group, Phys. Rev. D66, (2002) 010001-381.

[11] D.N. Spergel et al., Astrophys. J. Suppl. 148 (2003) 175.

[12] M. Maltoni et al., arXiv:hep-ph/0405172.

[13] http://www-boone.fnal.gov/

[14] L. Wolfenstein, Phys. Rev. D 17, (1978) 2369;
S.P. Mikheyev and A.Yu. Smirnov, Sov. J. Nucl. Phys. 42 (1986) 913.

[15] T. Doke, Nucl. Instrum. Meth. A 327 (1993) 113.

[16] W. J. Willis and V. Radeka, Nucl. Instr. & Meth. 120 (1974) 221.

[17] C. Rubbia, CERN-EP/77-08, (1977).

[18] E. Aprile, K. L. Giboni and C. Rubbia, Nucl. Instr. & Meth. A241 (1985) 62.

[19] P. Benetti et al., [ICARUS Collaboration], Nucl. Instr. & Meth. A332 (1993) 395.

[20] P. Cennini et al., [ICARUS Collaboration], Nucl. Instr. & Meth. A345 (1994) 230.

[21] F. Arneodo et al., [ICARUS Collaboration], arXiv:hep-ex/9812006.

[22] S. Amerio et al., [ICARUS Collaboration], Nucl. Instr.& Meth. A527 (2004) 329.

[23] S. Amoruso et al., [ICARUS Collaboration], The European Physical Journal C, Eur. Phys. J. C 33 (2004) 233.

[24] S. Amoruso et al., [ICARUS Collaboration], Nucl. Instr.& Meth. A523 (2004) 275.

[25] M. Antonello et al., [ICARUS Collaboration], Nucl. Instr.& Meth. A517 (2004) 348.

[26] S. Amoruso et al., [ICARUS Collaboration], Nucl. Instr.& Meth. A516 (2004) 68.

[27] F. Arneodo et al., [ICARUS Collaboration], Nucl. Instr. & Meth. A508 (2003) 287.

[28] P. Aprili et al., [ICARUS Collaboration], LNGS-EXP 13/89 add.2/01, and CERN-SPSC-2002-027.

[29] A. Ereditato and A. Rubbia, "Ideas for future liquid argon detectors," Proceedings of the Third International Workshop on Neutrino-Nucleus Interactions in the Few GeV Region, NUINT04, March 2004, Gran Sasso, Italy, Nucl. Phys. Proc. Suppl. 139 (2005) 301 [arXiv:hep-ph/0409143].

[30] K. Nitta et al., Nucl. Instr & Meth. A535 (2004) 147.

[31] M. Antonello et al., Nucl. Instr. & Meth. A516 (2004) 348.

[32] W.F. Schmidt, Trans. Electrical Insulation EI-19, 389 (1984).

[33] R. E. Kalman, Trans. ASME, J. Bas. Eng. 82D (1960).

[34] R. Fruhwirth, Nucl. Instrum. Meth. A **262** (1987) 444.

[35] P. Lipari, Nucl. Phys. Proc. Suppl. **112**, 274 (2002).

[36] See, for example, talks given at NuINT04 (http://nuint04.lngs.infn.it)

[37] See, for example, talks given at NuINT04 (http://nuint04.lngs.infn.it)

[38] E. A. Paschos and A. V. Kartavtsev, hep-ph/0309148; J. Marteau *et al.*,hep-ph/9906449.

[39] See, for example, B. Adeva *et al.*, Phys. Lett. **B412**, 414 (1997).

[40] L. A. Ahrens *et al.*, Phys. Rev. **D35**, 785 (1987).

[41] W. M. Alberico, S. M. Bilenky and C. Maieron, AIP Conf. Proc. **721**, 350 (2004) [arXiv:hep-ph/0311053].